OPEN ACCESS



ALMA Observations of Fragmentation, Substructure, and Protostars in High-mass Starless Clump Candidates

Brian E. Svoboda^{1,2,10}, Yancy L. Shirley^{2,11}, Alessio Traficante^{3,4}, Cara Battersby^{5,6}, Gary A. Fuller⁴, Qizhou Zhang⁶, Henrik Beuther⁷, Nicolas Peretto⁸, Crystal Brogan⁹, and Todd Hunter⁹, National Radio Astronomy Observatory, 1003 Lopezville Rd, Socorro, NM 87801, USA; bsvoboda@nrao.edu

Steward Observatory, University of Arizona, 933 North Cherry Avenue, Tucson, AZ 85721, USA

JAPS-INAF, via Fosso del Cavaliere, 100, 1-00133, Roma, Italy

Jodrell Bank Centre for Astrophysics, The School of Physics and Astronomy, The University of Manchester, Oxford Road, Manchester M13 9PL, UK

Department of Physics, University of Connecticut, 2152 Hillside Road, Storrs, CT 06269, USA

Harvard-Smithsonian Center for Astrophysics, 60 Garden Street, Cambridge, MA 02138, USA

Max Planck Institute for Astronomy, Königstuhl 17, D-69117 Heidelberg, Germany

School of Physics & Astronomy, Cardiff University, Queen's building, The parade, Cardiff, CF24 3AA, UK

National Radio Astronomy Observatory, 520 Edgemont Road, Charlottesville, VA 22903, USA

Received 2018 September 25; revised 2019 August 24; accepted 2019 August 26; published 2019 November 15

Abstract

The initial physical conditions of high-mass stars and protoclusters remain poorly characterized. To this end, we present the first targeted ALMA Band 6 1.3 mm continuum and spectral line survey toward high-mass starless clump candidates, selecting a sample of 12 of the most massive candidates $(4 \times 10^2 M_{\odot} \lesssim M_{cl} \lesssim 4 \times 10^3 M_{\odot})$ within $d_{\odot} < 5$ kpc. The joint 12 + 7 m array maps have a high spatial resolution of $\lesssim 3000$ au (0.015 pc, $\theta_{\rm syn} \approx 0.000$ and have high point-source mass-completeness down to $M \approx 0.3$ M_{\odot} at $6\sigma_{\rm rms}$ (or $1\sigma_{\rm rms}$ column density sensitivity of $N = 1.1 \times 10^{22} \,\mathrm{cm}^{-2}$). We discover previously undetected signposts of low-luminosity star formation from CO $J=2 \rightarrow 1$ and SiO $J=5 \rightarrow 4$ bipolar outflows and other signatures toward 11 out of 12 clumps, showing that current MIR/FIR Galactic plane surveys are incomplete to low- and intermediate-mass protostars ($L_{\rm bol} \lesssim 50 \, L_{\odot}$), and emphasizing the necessity of high-resolution follow-up. We compare a subset of the observed cores with a suite of radiative transfer models of starless cores. We find a high-mass starless core candidate with a model-derived mass consistent with $29_{15}^{52} M_{\odot}$ when integrated over size scales of $R < 2 \times 10^4$ au. Unresolved cores are poorly fit by radiative transfer models of externally heated Plummer density profiles, supporting the interpretation that they are protostellar even without detection of outflows. A high degree of fragmentation with rich substructure is observed toward 10 out of 12 clumps. We extract sources from the maps using a dendrogram to study the characteristic fragmentation length scale. Nearest neighbor separations, when corrected for projection with Monte Carlo random sampling, are consistent with being equal to the clump average thermal Jeans length ($\lambda_{i,th}$; i.e., separations equal to 0.4–1.6 \times $\lambda_{i,th}$). In the context of previous observations that, on larger scales, see separations consistent with the turbulent Jeans length or the cylindrical thermal Jeans scale $(\approx 3-4 \times \lambda_{i,th})$, our findings support a hierarchical fragmentation process, where the highest-density regions are not strongly supported against thermal gravitational fragmentation by turbulence or magnetic fields.

Key words: ISM: clouds - ISM: molecules - ISM: structure - stars: formation

1. Introduction

High-mass stars ($M_*>8\,M_\odot$) strongly influence the evolution of galaxies and the ISM, yet many fundamental questions remain to be answered concerning the incipient phases of high-mass star formation (e.g., Beuther et al. 2007; Tan et al. 2014; Motte et al. 2018). Observational constraints on the initial physical conditions of protocluster evolution are a necessary prerequisite to improved understanding of high-mass star and cluster formation. Of particular importance are observations of the quiescent environments before the initial conditions are disrupted by the extreme radiative and mechanical feedback of high-mass stars. Thus, our understanding of both how cluster formation is initiated and the ensuing protocluster evolution

Original content from this work may be used under the terms of the Creative Commons Attribution 3.0 licence. Any further distribution of this work must maintain attribution to the author(s) and the title of the work, journal citation and DOI.

depend on identifying and constraining the physical properties of representative samples of starless molecular cloud "clumps." ¹²

Recent blind surveys of dust continuum emission at (sub-) millimeter and far-infrared (FIR) wavelengths of the Galactic plane have identified large statistical samples of clumps, enabling the discovery of those in the earliest evolutionary phases. Such surveys include the Bolocam Galactic Plane Survey¹³ (BGPS; Rosolowsky et al. 2010; Aguirre et al. 2011; Ginsburg et al. 2013) at 1.1 mm, ATLASGAL¹⁴ at 870 μ m (Schuller et al. 2009; Contreras et al. 2013; Csengeri et al. 2014), JCMT Galactic Plane Survey¹⁵ at 850 μ m (Eden et al. 2017, JPS), and

¹⁰ Jansky Fellow of the National Radio Astronomy Observatory.

¹¹ Adjunct Astronomer of the National Radio Astronomy Observatory.

 $[\]overline{^{12}}$ In this paper, we use the term "core" to refer to a dense gas structure that is ~ 0.1 pc in size and likely to form a single or bound multiple stellar system. Such cores are embedded within larger-scale "clumps" that are dense gas structures likely to form a stellar association or cluster, and are ~ 1 pc in size and $\sim 10^2 - 10^4 \, M_{\odot}$ in mass (see Bergin & Tafalla 2007).

¹³ Data products can be downloaded from https://irsa.ipac.caltech.edu/data/BOLOCAM_GPS/.

http://www3.mpifr-bonn.mpg.de/div/atlasgal/

¹⁵ http://apps.canfar.net/storage/list/JPSPR1

Herschel Hi-GAL at 70, 160, 250, 350, and 500 μ m (Molinari et al. 2010, 2016). Starless clump candidates (SCCs) are identified by cross-matching clump catalogs to catalogs of star formation indicators and selecting clumps unassociated with any indicators. These indicators include 70 μ m compact sources, color-selected young stellar objects (YSOs), H₂O and CH₃OH masers, and UCHII regions in Svoboda et al. (2016) for the BGPS and in Yuan et al. (2017) for ATLAS-GAL, in total identifying more than $\gtrsim 2 \times 10^3$ SCCs in the inner Galaxy. In addition, more than $\gtrsim 10^4$ clumps without 70 μ m sources have been identified from the Hi-GAL survey (Traficante et al. 2015; Elia et al. 2017). In this study, we aim to systematically study a representative sample of the highestmass SCCs within 5 kpc in order to understand the fragmentation characteristics at high spatial resolution, identify potential high-mass starless cores ($M \gtrsim 30 M_{\odot}$, $R \lesssim 0.1 \text{ pc}$), and search for previously undetected low-luminosity protostellar activity.

A variety of physics, including thermal gas pressure, turbulence, magnetic fields, and the geometry of filaments and density gradients, likely play a role in the fragmentation of molecular clouds and the resultant dense core populations. Recent high-resolution observations with millimeter and submillimeter interferometers of high-mass clumps with little sign of star formation reveal significant fragmentation at the early stage of cluster formation (Zhang et al. 2009, 2015; Wang et al. 2011, 2012, 2014; Zhang & Wang 2011; Beuther et al. 2015b; Lu et al. 2015; Sanhueza et al. 2017). These studies found that the most massive fragments in the clumps are at least ten times greater than the thermal Jeans mass, indicating that additional support from turbulence and/or magnetic fields are required. Most of these studies focused on individual clumps and typically have not had the sensitivity to adequately detect fragments of a thermal Jeans mass (detections of $\gtrsim 2 M_{\odot}$ at $4\sigma_{\rm rms}$). In contrast, the fragmentation scales in nearby molecular clouds have been studied extensively with recent notable analyses toward Serpens (Friesen et al. 2017), the Orion Integral Shaped Filament (Kainulainen et al. 2017), and Perseus (Pokhrel et al. 2018). These studies find support for hierarchical, scale-dependent fragmentation with separations corresponding to a range between thermal Jeans fragmentation and thermal filamentary gravitational fragmentation. It is not understood how these results extend toward earlier evolutionary stages in massive SCCs, which are the focus of this work.

Publicly available millimeter and FIR Galactic plane survey observations do not have sufficient angular resolution at $\sim 20''$ 30'' (~ 0.5 pc at 4 kpc) to study the substructure and dense core properties in distant SCCs. For example, the high-mass prestellar core candidate G028-C1S ($M_c \sim 60 M_{\odot}$) studied in Tan et al. (2013) was only identified as protostellar until interferometric follow-up of outflow tracers (Feng et al. 2016; Tan et al. 2016). High-mass SCCs remain largely unstudied at high spatial resolution, owing to the historical difficulty in identification and typically large heliocentric distances, with only a handful of studies on individual objects to date (Beuther et al. 2015a; Sanhueza et al. 2017). In particular, the high-mass starless clump candidate "MM1" of IRDC G28.23-0.19 (Sanhueza et al. 2013) has been studied in detail to determine that it is devoid of star formation indicators, including 3.6-70 μ m point sources, H₂O and CH₃OH masers (Wang et al. 2006; Chambers et al. 2009), and radio continuum (Battersby et al. 2010; Rosero et al. 2016). The global physical properties of G28.23–0.19 MM1 (corresponding to BGPS catalog clump number 4649) are similar to the average properties of the SCCs presented in this work. G28.23–0.19 MM1 is high-mass, cold, compact, and dense (i.e., $M_{\rm cl} \approx 1.5 \times 10^3 \, M_{\odot}$, $T_{\rm K} \approx 12$ K, R = 0.6 pc, $n \approx 3 \times 10^4$ cm⁻³; Sanhueza et al. 2017). However, it represents only a single clump, and the sensitivity and sample size of the dense cores are not sufficient for a precise measurement of the fragmentation scale. In this survey, we present observations on a sample of 12 clumps that are selected from a blind Galactic plane survey and are among the most massive SCCs.

Existing large samples of SCCs have been primarily identified through the nondetection of coincident Hi-GAL 70 μ m sources (Veneziani et al. 2013; Traficante et al. 2015; Svoboda et al. 2016; Elia et al. 2017), which is less affected than shorter wavelength 8 μ m or 24 μ m observations by both local extinction and from contamination of evolved stars (principally those on the asympototic giant branch). The completeness of the 70 μ m maps to protostar bolometric luminosity, L_{bol} , is affected by the survey depth and complex structure in the foreground and background emission that hinders the clear identification of compact sources. Svoboda et al. (2016) calculate the $L_{\rm bol}$ completeness function for Hi-GAL 70 μ m compact sources associated with BGPS clumps and the respective distribution of heliocentric distances. They find that, for clumps with low $70 \,\mu\mathrm{m}$ backgrounds $(\sim 500-1000 \text{ MJy sr}^{-1})$, the 90% completeness limit is $L_{\rm bol} = 50 \, L_{\odot}$ (see Section 3.2.4 in Svoboda et al. 2016), which is greater than \gtrsim 95% of YSOs in the Gould's Belt (n. b. median $1L_{\odot}$; Dunham et al. 2014). Faint 24 μ m sources coincident with the clump column density peaks toward 9/18 of 70 μ m dark SCCs suggest likely embedded intermediatemass star formation that is undetected in the Hi-GAL observations (Traficante et al. 2017). However, it is currently unknown what degree of star formation has been initiated, if at all, in SCCs without sensitive and unambiguous tracers of protostellar activity, such as bipolar molecular outflows. Systematic observations of SCCs at high resolution are necessary to determine what (if any) degree of low-luminosity star formation has begun in SCCs, with important implications for the protostellar accretion history.

The principal theories of high-mass star formation in dense Galactic molecular cloud clumps are the monolithic collapse of turbulent cores in virial equilibrium (McKee & Tan 2002, 2003; Hosokawa & Omukai 2009) and the accretion of subvirial cores through gravitationally driven cloud inflow (Smith et al. 2009; Hartmann et al. 2012). The latter replace the competitive Bondi-Hoyle accretion of cores (Bonnell et al. 2001; Wang et al. 2010) with cores being fed the gas reservoir through inflowing streams. The turbulent core model predicts monolithic high-mass starless cores, whereas the competitive model predicts a fragmentation of cores near the thermal Jeans mass. The existence of high-mass starless cores is a key distinction between these models-yet few, if any, observational candidates are known (Kong et al. 2017), and some promising candidates (e.g., G028-C1S) have revealed embedded protostellar activity upon further observational investigation (Tan et al. 2013, 2016; Feng et al. 2016). Irrespective of the specific theoretical model, measurements of the fragmentation properties at early evolutionary phases

Table 1
Target Positions

Name	ℓ (deg)	b (deg)	α (ICRS) (h:m:s)	δ (ICRS) (d:m:s)	$(\operatorname{km}^{v_{\operatorname{lsr}}})$	BGPS ID ^a
G22695	22.695381	-0.454657	18:34:14.58	-09:18:35.84	77.80	3686
G23297	23.297388	0.055330	18:33:32.06	-08:32:26.27	55.00	3822
G23481	23.479544	-0.534764	18:35:59.56	-08:39:02.53	63.80	3892
G23605	23.605390	0.181325	18:33:39.40	-08:12:33.24	87.00	3929
G24051	24.051381	-0.214655	18:35:54.40	-07:59:44.60	81.10	4029
G28539	28.538652	-0.270358	18:44:22.60	-04:01:57.70	88.60	4732
G28565	28.527846	-0.252172	18:44:17.52	-04:02:02.40	87.46	4729
G29558	29.557855	0.185321	18:44:37.07	-02:55:04.40	79.72	5021
G29601	29.604891	-0.576768	18:47:25.20	-03:13:26.04	75.78	5030
G30120	30.119855	-1.146674	18:50:23.54	-03:01:31.58	65.31	5114
G30660	30.657875	0.044680	18:47:07.76	-02:00:12.17	80.20	5265
G30912	30.913113	0.720803	18:45:11.28	-01:28:03.72	50.74	5360

Note.

provide valuable observational constraints on the initial physical conditions of high-mass star and cluster formation. To this end, we perform a systematic search for high-mass starless cores toward massive SCCs with the Atacama Large Millimeter/submillimeter Array.

In this paper, we present a systematic survey of 12 high-mass SCCs at subarcsecond resolution. We present our sample selection, observational setup, and data reduction methodology in Section 2. We describe detections of previously unknown, low-luminosity protostellar activity in Section 3 and the modeling of continuum sources in Section 4. We measure and analyze the fragmentation scale between sources in Section 5, discuss the implications in Section 6, and report our conclusions in Section 7. In Appendix C, we include a detailed description of the setup and computation of radiative transfer models analyzed in Section 4.

2. Observations

2.1. Sample Selection

We have identified SCCs through the combined catalogs and images of primarily two dust continuum Galactic plane surveys: (1) an evolutionary analysis of BGPS 1.1 mm (Svoboda et al. 2016, hereafter \$16), and (2) comparison of the Peretto & Fuller (2009) infrared dark cloud (IRDC) catalog with Hi-GAL images (Traficante et al. 2015). The BGPS observed between $-10^{\circ} < \ell < 90^{\circ}$ with |b| < 0.5 (expanding to |b| < 1.5 for selected ℓ) at $\lambda_c = 1.12$ mm with a $\theta_{hpbw} = 33''$ synthesized angular resolution. In the region $10^{\circ} < \ell < 65^{\circ}$, the BGPS has been compared to a diverse set of a observational indicators for star formation activity (S16). These indicators include compact 70 μ m sources, mid-IR color-selected YSOs, H2O masers, Class II CH3OH masers, extended 4.5 μ m outflows, and UCHII regions. From the sample of more than 2500 SCCs in the combined samples of S16 and Traficante et al. (2015), we target the 12 highestmass SCCs within d_{\odot} < 5 kpc. Point sources at 70 μ m were identified by visual inspection in S16 and by an automated extraction in Traficante et al. (2015). Three clumps (G28565, G29601, and G309120), which were initially determined from the automated extraction to be dark at 70 μ m, show association with weak sources upon closer scrutiny by visual inspection. Among the 12 ALMA targets, nine have no detectable point-source emission from Hi-GAL 70 μ m (flag 0 in S16), two have low-confidence or marginal detections (flag 4, G28565 and G29601), and one has bright, compact detection (flag 1, source G30912). We emphasize that starless clump candidates are designated based on the observational data sets and identification techniques used, and that these factors are reflected in the completeness and purity of the resulting catalogs of SCCs. Table 1 details the target positions and velocities. Table 2 details the physical properties of the sample, and Figure 1 shows images of the clumps at wavelengths from 8 μ m to 350 μ m.

The clump average physical properties in S16 are shown in Figure 2, plotting peak mass surface density $\Sigma_{\rm cl,pk}$ (at $\theta_{\rm hpbw}=33''$) and total mass $M_{\rm cl}$, for sources with well-constrained distances less than $d_{\odot}<5$ kpc and $10^{\circ}<\ell<65^{\circ}$. Protostellar clumps and SCCs are plotted, where SCCs have quiescent background emission and no detected compact sources from the Hi-GAL 70 μ m images (flag 0; see Section 3.2.4 of S16). Protostellar clumps are typically higher in both mass and mass surface density compared to SCCs. The ALMA targets are shown, occupying the highest $\Sigma_{\rm cl,pk}$ and $M_{\rm cl}$ portions of the SCC distribution where typical values for the sample are $M_{\rm cl}\sim 800~M_{\odot}$ and $\Sigma_{\rm cl,pk}\sim 0.1~{\rm g~cm^{-2}}$ (measured over $\sim 0.6~{\rm pc}$ scales). In particular, G28539 stands out as the most massive clump in the sample at $M_{\rm cl}\sim 3\times 10^3~M_{\odot}$, and also as having the highest peak mass surface density.

Assuming a star formation efficiency of $\epsilon_{\rm sf}=0.3$ and a standard stellar initial mass function (IMF; Kroupa 2001), a $320\,M_\odot$ clump meets the criteria to form a $8\,M_\odot$ star (see Section 6.1 of S16). All of the clumps that comprise this sample are above this mass threshold, and are similarly above the mass–radius relationship for high-mass star formation proposed by Kauffmann & Pillai (2010). In practice, however, it is difficult to assess the high-mass star formation potential of clumps beyond these simple heuristics. It should be kept in mind that, if the star formation efficiency of the targets

^a Catalog ID number in the BGPS v2.1.0 (Ginsburg et al. 2013).

 $[\]overline{^{16}}$ Kauffmann & Pillai (2010) define the prescription $M \le 580 \, M_{\odot} (R/\mathrm{pc})^{1.33}$ for a clump to form high-mass stars. The prefactor has been scaled for consistency with the dust opacity used in this work. For radius R=0.8 pc, this relation yields a mass threshold of $M \approx 430 \, M_{\odot}$.

Table 2Clump Physical Properties

Name	d_{\odot}	$\Sigma_{ m pk}$	M_{cl}	$T_{\rm K}$
	(kpc)	(g cm ⁻²)	(M_{\odot})	(K)
G22695	4450 (190)	0.0580 (0.013)	930 (110)	14.70 (0.42)
G23297	3480 (281)	0.0760 (0.019)	420 (85)	11.73 (0.41)
G23481	3780 (220)	0.1100 (0.024)	760 (120)	11.29 (0.14)
G23605	4800 (240)	0.0370 (0.015)	880 (260)	()
G24051	4490 (210)	0.0790 (0.015)	760 (110)	11.87 (0.37)
G28539	4780 (220)	0.1280 (0.011)	3610 (360)	12.38 (0.14)
G28565	4680 (200)	0.0830 (0.019)	910 (220)	()
G29558	4370 (240)	0.0690 (0.014)	590 (86)	12.11 (0.17)
G29601	4270 (280)	0.0900 (0.018)	660 (130)	15.98 (0.27)
G30120	3680 (260)	0.0750 (0.031)	820 (160)	14.12 (0.15)
G30660	4410 (240)	0.0770 (0.019)	1380 (360)	()
G30912	2980 (250)	0.0990 (0.019)	450 (88)	11.67 (0.12)

Note. Uncertainties are reported as the MAD in parentheses. Properties are taken from Svoboda et al. (2016), except for mass measurements of G29601 and G30912, which are taken from Traficante et al. (2015).

is substantially lower than the typical assumed value of $\epsilon_{\rm sf}=0.3$, then they are unlikely to form high-mass stars.

2.2. ALMA Band 6

As part of Atacama Large Millimeter/submillimeter Array (ALMA) Cycle 3 program 2015.1.00959.S, we observed 12 clumps in Band 6 in a compact configuration (C36-2; joint 12 + 7 m array baselines range from ~ 9 to 450 m). Data were taken between 2016 March 3 and 20 for the 12 m array, and between 2016 April 30 and August 19 for the 7 m array. Including time for calibration and overheads, the 12 m array observations lasted for approximately 12 hr, with typical precipitable water vapor of 1.5 mm. Titan and J1733-1304 were used as flux calibrators, J1751+0939 to calibrate the bandpass, and J1743-0350 and J1830+0619 to calibrate the timedependent gains. Identical 1 hr scheduling blocks were configured to interleave and observe all 12 targets within the same block, and because sources are within a 5° radius on the sky (22.7 < $\ell < 30^{\circ}9$), the same calibrators can be used. Thus, due to their nearly identical observing conditions, the individual maps have similar uv-coverage, atmospheric noise, and beam size.

Positions for the sample were chosen from the BGPS 1.1 mm continuum peak flux density position and compared for consistency with the ATLASGAL 870 μ m peak emission and Hi-GAL 70 μ m peak absorption (when present) positions. The Band 6 receiver was configured in dual-polarization mode, with lower and upper sidebands centered near 215 and 230 GHz, respectively. The observations targeted each clump peak with a single pointing with half-power beamwidth (HPBW) of the measured primary beam 26."6 (~0.5 pc at $d_{\odot} = 4$ kpc) and 20%-power beamwidth of 40" (~0.8 pc), the effective limit of the 12 m array field of view.

2.2.1. ALMA 1.3 mm Continuum Reduction

Data reduction was performed using CASA (version 4.7.134-DEV, r38011, for consistency with QA2 delivered products). Line-free continuum visibilities were created by flagging channels contaminated by spectral lines, where the input spectral windows (SPWs) were further visually inspected to check for emission at unexpected velocity ranges, partitioned out into a new measurement set with the split task, and

channel averaged to 25 MHz in order to avoid bandwidth smearing. Together, this yields ≈ 3.5 GHz of dual-polarization continuum bandwidth. The continuum image root mean square (rms; $\sigma_{\rm rms} = \sqrt{\sum_n I_n^2/n}$) is measured for each CLEANed image within a region that excludes identified emission using the casaviewer tool. None of the images are limited in dynamic range, with peak image intensity divided by the rms less than 200. We estimate the fiducial mass sensitivity given $T_{\rm K}({\rm NH_3}) \approx 12~{\rm K}$, thermally coupled gas and dust $(T_{\rm d}=T_{\rm K})$, and OH5 dust opacity $\kappa(\lambda = 1.3 \text{ mm}) = 0.899 \text{ cm}^2 \text{ g}^{-1}$). The methods for deriving dust mass values from the continuum emission are discussed in more detail in Section 4. The joint 12 + 7 m continuum was then iteratively CLEANed with manual masking via the tclean task, using the multiscale deconvolver and a robust weighting of 1, down to a brightness threshold of $2-3\sigma_{\rm rms}$. An image cell size of 0."1 was used for all continuum and spectral line maps. Self-calibration was not applied, because the brightest sources in the image are only a few mJy and not bright enough for a conservative self-cal to produce a noticeable improvement without also increasing the image noise. The resultant images have a synthesized beam size of $\theta_{maj}\approx 0\rlap.{''}85$ by $\theta_{min}\approx 0\rlap.{''}75$ (0\rlap.{''}8 angular diameter yields 2800–3800 au at $d_{\odot} = 3.5$ –4.8 kpc). The continuum images are shown in Figure 3.

2.2.2. ALMA Spectral Line Reduction

The flexibility of the ALMA correlator enabled simultaneous observation of several molecular line transitions. Table 3 reports the details of the correlator configuration. We observed nine SPWs with one wide-band, low-spectral resolution window centered at 233.8 GHz and eight high-spectral resolution windows centered on lines of interest. Table 4 reports the transition quantum numbers, rest frequencies, and upper energy levels ($E_{\rm u}/k$). The SPWs containing the H₂CO and CH₃OH transitions have a spectral resolution of 0.34 km s^{-1} , and the other line SPWs have 0.68 km s^{-1} resolution. Line rest frequencies were taken from a combination of the SLAIM¹⁷ (Remijan et al. 2007; F. J. Lovas 2019, private communication) and the CDMS (Müller et al. 2005) online spectroscopic databases. The line SPWs from the 12 + 7 m arrays were jointly imaged using the CASA task tclean, with a Briggs robust parameter of 1.0 and a cell size of 0",1, and regridded to common spectral resolutions listed in Table 4. We find typical rms noise levels in the image cubes of $1.8 \text{ mJy/(km s}^{-1})$ (i.e., 2.2 mJy per 0.68 km s^{-1} channel or $3.0 \text{ mJy per } 0.34 \text{ km s}^{-1} \text{ channel}) \text{ or } 71 \text{ mK/(km s}^{-1}) \text{ when}$ converted to brightness temperature units (HPBW beam size of 0.85×0.75).

In this work, we inspect the line image cubes for detection of emission, as well as for the presence of outflows traced by CO and SiO, but we do not CLEAN the data cubes. Due to the lack of full uv-coverage, the CO maps in particular show strong effects of spatial filtering near the systematic velocities that make the deconvolution process complex and error-prone. Detailed analysis of the spectral line data is left to a future work. Table 6 lists the detection flags per target for the continuum, molecular lines, and outflows. Features are considered detections if they have peak intensities $\geqslant 7\sigma_{\rm rms}$ ("D"), weak detections if between 5 and $7\sigma_{\rm rms}$ ("W"), and

http://splatalogue.net

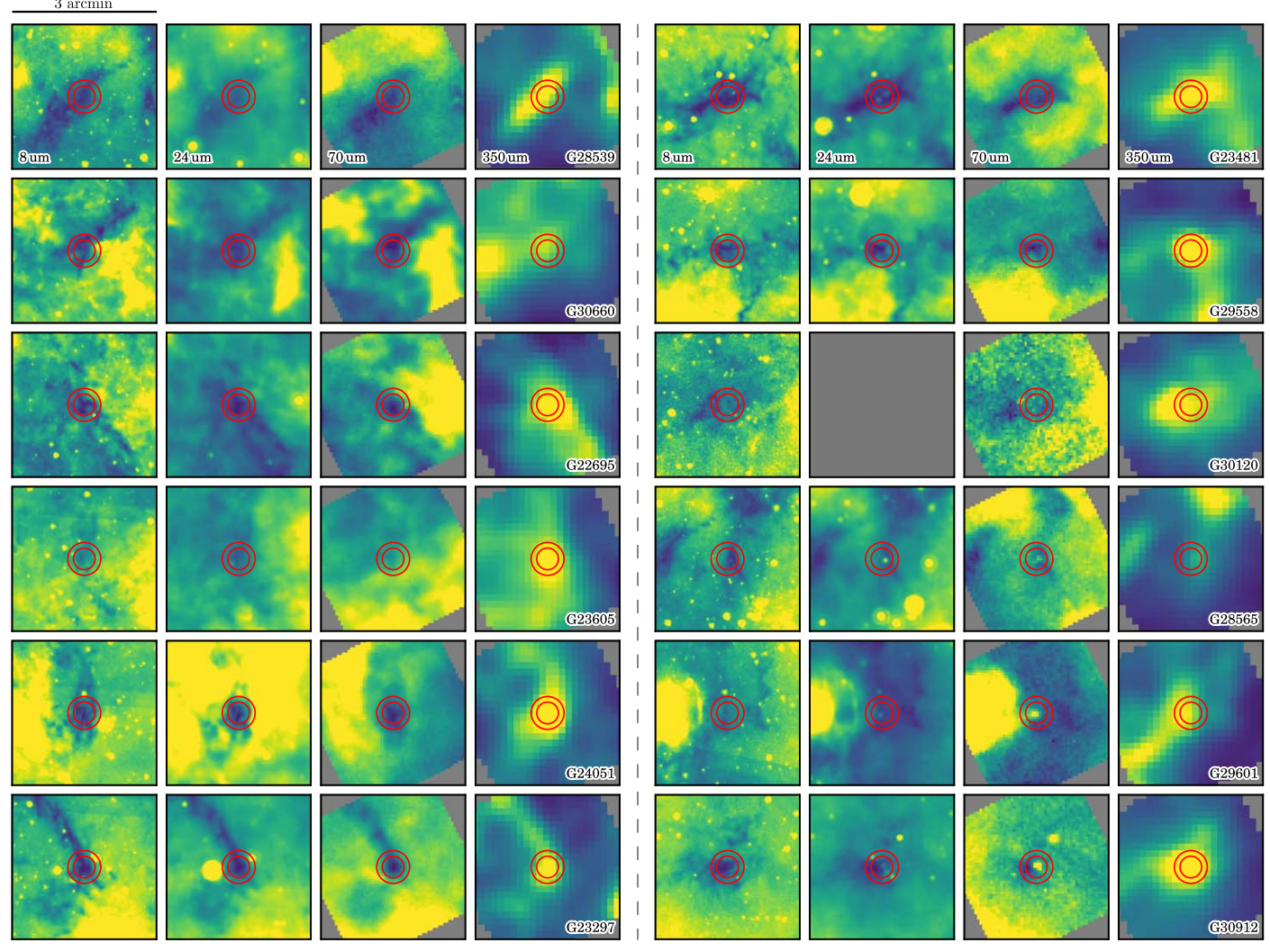


Figure 1. Mid- and far-infrared $3' \times 3'$ maps of the clumps in the survey sample, showing GLIMPSE 8 μ m, MIPSGAL 24 μ m, and Hi-GAL 70 μ m and 350 μ m. The ALMA Band 6 single pointings target the peak flux positions derived from the BGPS 1.1 mm observations. The inner and outer red circles show the 50% (27") and 20% (40") power points of the primary beam for the ALMA 12 m array images. Clumps from Svoboda et al. (2016) were selected to have no detected indicators of star formation activity, such as embedded 70 μ m sources, H₂O or CH₃OH masers, or UCHII regions. Clumps from Traficante et al. (2015) were selected to be 70 μ m dark using an automated extraction, one of which shows a marginal detection and two of which show clear detections upon visual inspection. Note that G30120 at $b \approx -1$ °.1 is outside the MIPSGAL survey and does not contain *Spitzer* 24 μ m data.

nondetections if $\leq 5\sigma_{rms}$. Targets that exhibit bipolar outflows in CO or SiO are flagged "B" (discussed below in Section 3.2).

2.3. Image Fidelity and MIR Comparison

The dense gas features revealed in the continuum maps clearly show hierarchical structure, with bright ridges, filaments, and cores contained within larger features with lower surface brightness. Given the complexity within the maps and the systematic uncertainties of imaging, we compare the continuum images to an additional measure of gas column density at comparable resolution, MIR extinction. For appropriate configurations of distance and the MIR radiation field, clumps can appear associated with 8 μ m absorption features (EMAFs), where high column densities at close distances typically yield the strong MIR shadows that identify infrared dark clouds (IRDCs). MIR extinction mapping has the advantages of comparatively high resolution, insensitivity to dust temperature, and lack of spatial filtering. We use the

Spitzer GLIMPSE (Benjamin et al. 2003; Churchwell et al. 2009) IRAC Band 4 ($\lambda_c = 7.9~\mu m$, 2" FWHM) mosaic to show the EMAF contrast. Figure 4 presents a map of the flux density S_8 with the ALMA 230 GHz continuum for source G24051 overlaid. The dense gas structures observed in the millimeter continuum show a remarkable consistency when compared with the column density features inferred from the MIR contrast. This holds similarly true for the other clumps in the sample, as all show at least some MIR extinction. Qualitatively this good correspondence supports the fidelity of the emission structure detected in the ALMA maps.

2.4. Core Identification and Dendrogram

In order to analyze the fragmentation scale, we first identify dense gas substructures using a segmentation algorithm. The nature of the tree data structure in the dendrogram algorithm makes it well-suited to identifying and categorizing structure in images with hierarchical structure (see Rosolowsky et al. 2008),

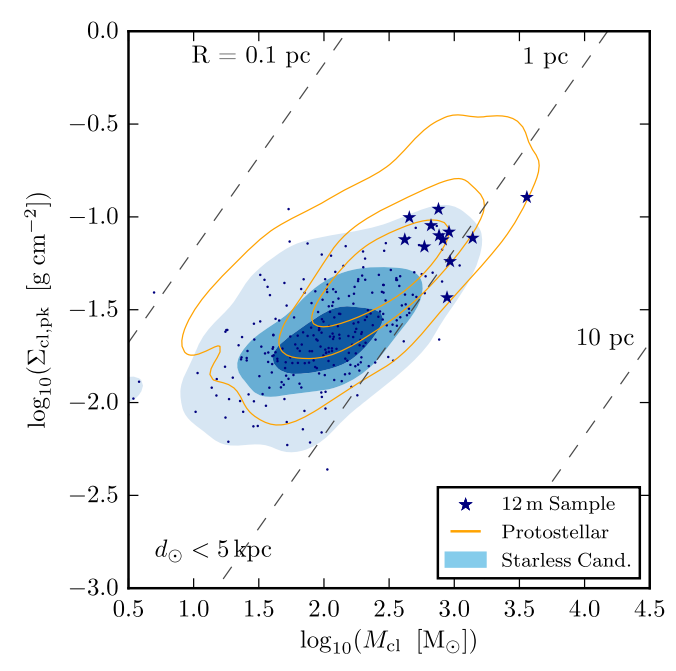


Figure 2. Peak mass surface density $\Sigma_{\rm cl,pk}$ vs. total mass $M_{\rm cl}$. Values are derived from the BGPS at 1.1 mm ($\theta_{\rm hpbw}=33''$) for clumps with well-constrained distances $d_{\odot}<5$ kpc. Starless clump candidates are represented by blue points and contours, protostellar clumps by orange contours, and the ALMA sample by blue stars. Total masses of the sample range between $M_{\rm cl}\approx400-3000\,M_{\odot}$ and $\Sigma_{\rm cl,pk}\sim0.1$ g cm $^{-2}$. The dashed lines show $\Sigma_{\rm cl,pk}$ as a function of $M_{\rm cl}$ for constant radii at 0.1 pc, 1.0 pc, and 10 pc.

as opposed to a simpler segmentation algorithms, such as that done with a seeded watershed algorithm (e.g., CLUMPFIND; Williams et al. 1994). We use the open source Python software library astrodendro to create the dendrogram and catalog of cores. The dendrogram has three principal tunable parameters: a minimum threshold value, v_{min} , that sets the floor or outer boundary of each tree; the minimum contrast or step size, δ_{step} , between nodes; and the minimum area, Ω_{\min} . Because the noise varies considerably across the primary beam of each image, we apply the dendrogram to maps that have not been corrected for the weight of the primary beam. This effectively works to identify features with outer contours of constant statistical significance across the field of view, rather than outer contours of constant flux. Sources are extracted out to the limit of the maps, set to the 20% power point of the primary beam. We choose conservative values for each parameter, using $v_{\rm min} = 3\sigma_{\rm rms}$, $\delta_{\rm step} = 3\sigma_{\rm rms}$, and $\Omega_{\rm min} = \Omega_{\rm bm}$, applied to the unmasked images. Sources (i.e., leaves, or nodes without children) are then subselected to meet the criterion that the peak flux is $>5\sigma_{\rm rms}$. In total, we identify 67 substructures for the sample of 12 clumps. Figure 5 shows the dendrogram-extracted dense gas substructures in each clump. Table 5 catalogs the measured positions, sizes, and flux densities of the substructures. We find an average number of substructures per clump of $N_{\rm src} = 5.6$ (median 6), with the maximum ($N_{\rm src} = 11$) in G24051 and minimum ($N_{\rm src} = 1$) in G23605. G23605 is the only clump with $N_{\rm src} < 3$, and thus is not included in the source nearest neighbor distance analysis. Figure 6 presents $N_{\rm src}$ per clump versus $\Sigma_{cl,pk}$. A tentative increasing trend can be observed, in that clumps with high $\Sigma_{\text{cl,pk}}$ are more fragmented than lower $\Sigma_{cl,pk}$.

In principle, the distribution of integrated flux densities can be analyzed to measure a CMF, but in practice, there are large

observational uncertainties that complicate its interpretation. The principal contributor arises from at least a factor of three uncertainty in $T_d \sim 6-35 \text{ K}$ ($\sim 10 \times$ uncertainty in M), due to uncertainty in the ISRF, local extinction, and uncertainty in the protostellar activity of each source. Single-wavelength observations do not give us enough information to construct spectral energy distributions (SEDs) and measure average line-of-sight dust temperatures. Other significant systematics also arise from uncertainty in the missing flux density due to spatial filtering by the interferometer, dust opacity ($\delta \kappa / \kappa \approx 50\%$), kinematicderived heliocentric distance ($\delta d_{\odot}/d_{\odot} \approx 15\%$), and the aperture or source boundary used to extract S_{ν} . For these reasons, we shall leave the study of the characteristic fragmentation mass and the CMF in SCCs to a future work utilizing complementary NSF's Karl G. Jansky Very Large Array (JVLA) NH₃ observations that will provide both gas kinetic temperature and kinematic information (B. E. Svoboda et al. 2019, in preparation). The characteristic fragmentation length scale, on the other hand, can be inferred directly from the distribution of angular separations between sources, with assumptions on how to correct for geometric projection.

3. Protostellar Activity

In this section, we describe new evidence for protostellar activity. In Section 5, we perform an analysis of the fragmentation scale from the substructure detected in the continuum. With the improved sensitivity and resolution of ALMA, multiple indicators of protostellar activity are observed for the first time. In particular, bipolar molecular outflows detected in CO $J=2 \rightarrow 1$ and SiO $J=5 \rightarrow 4$ provide unambiguous evidence of embedded protostellar activity. The detection of molecular transitions with comparatively high upper excitation temperatures (*E*-CH₃OH $4_{2,2} \rightarrow 3_{1,2}$, $E_u/k=45.5$ K; p-H₂CO $3_{2,2} \rightarrow 2_{2,1}$, $E_u/k=68.1$ K) and detection of bright, compact continuum emission (unresolved on scales smaller than $\lesssim 3000$ au) are also suggestive of embedded, low- L_{bol} protostellar activity. Together, these data provide a clear indication of embedded protostars toward 11 out of 12 clumps.

3.1. Compact Continuum Sources

Numerous high signal-to-noise ratio (S/N, $S_{\nu}/\sigma_{\rm rms}$), point-like sources are observed in the continuum images (Figure 3). We speculate that such sources originate from the dense, centrally heated, inner envelopes of embedded protostars. In Section 4, we investigate whether the compact continuum sources are inconsistent with radiative transfer models of dense, starless cores.

We designate continuum sources as "compact" if they are unresolved or are marginally resolved on the scale of the ALMA synthesized beam $\theta_{\rm syn}\approx 0$."8. Continuum sources are determined to be unresolved if a Gaussian fit to the image plane data using the CASA task imfit reports an deconvolved angular sizes $\theta_{\rm dec}\lesssim \theta_{\rm syn}$. The deconvolved Gaussian FWHM are determined by subtracting the synthesized HPBW in quadrature from the fitted width, i.e., $\theta_{\rm dec}=\sqrt{\theta_{\rm fit}^2-\theta_{\rm syn}^2}$. These angular widths correspond to physical sizes of \lesssim 1500 au at heliocentric distances of $d_{\odot}\approx 4$ kpc. The brightest compact sources have typical peak flux densities between $S_{\rm 1.3,pk}\approx 1$ mJy beam $^{-1}$. All clumps aside from G28539 host a compact source with $S_{\rm 1.3,pk}>1$ mJy beam $^{-1}$. Indeed, sources G23605 and G30120 host compact sources, even though they

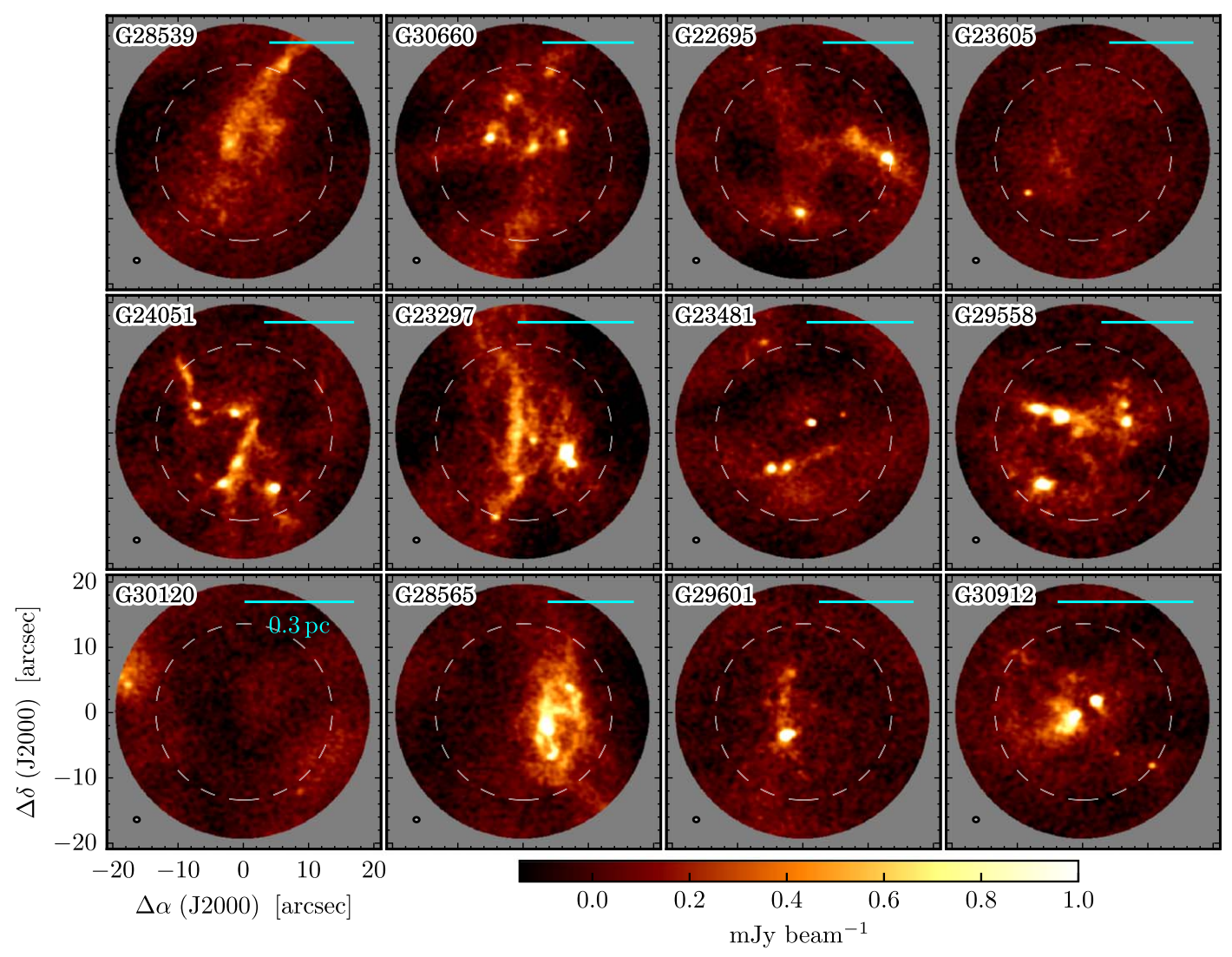


Figure 3. ALMA $12 + 7 \,\mathrm{m}$ array jointly deconvolved 230 GHz line-free continuum images. The clumps show a rich degree of fragmentation, with multiple condensations connected by filamentary structures, although sources G30120 and G23605 are largely devoid of detected emission on the scale of the synthesized beam $(0.0^{\prime\prime}.85 \times 0.0^{\prime\prime}.75)$, visualized at the lower left). The images are uncorrected for primary beam attenuation, for visual display purposes. The color scale ranges from -0.15 to 1.0 mJy beam $^{-1}$ on a linear scaling. The scale bar (cyan) visualizes 0.3 pc at the clump heliocentric distance. The dashed circle shows the half-power beamwidth $(27^{\prime\prime})$, and the image extends down to the 20% power point $(40^{\prime\prime})$.

show limited fragmentation otherwise. While lacking extended continuum emission, the compact source G23605 S1 has clear association with emission from multiple molecular species ($C^{18}O$, H_2CO , CH_3OH) at the LSR velocity of the clump, determined from the NH₃ emission (32", 0.7 pc resolution; S16). G30120 S1 is a compact source near the eastern edge of the field with a strong CO outflow and other molecular detections.

For comparison to nearby low-mass star-forming regions, Enoch et al. (2011) carried out a survey of Class 0 YSOs in Serpens at 230 GHz with CARMA. The envelope masses range between $M_{\rm env}=0.5$ –20 M_{\odot} (median $M_{\rm env}=3.7~M_{\odot}$) and with integrated flux densities between $S_{1.3}=1.4\times10^{1}$ –4.0 \times 10³ mJy (median $S_{1.3}=120$ mJy) and deconvolved size scales between D=400–3000 au (median $D\approx700$ au). With a heliocentric distance of $d_{\odot}=415\pm25$ pc to Serpens (Dzib et al. 2010), the 120 mJy median source flux density and 700 au size measured by Enoch et al. (2011) correspond to 1.2 mJy and 0.″18 when scaled to a fiducial distance of 4 kpc. If there

are low- to intermediate-mass Class 0 YSOs with physical properties in these SCCs similar to those in Serpens, then they would be consistent with the observed bright ($\gtrsim 20\sigma_{rms}$) unresolved point continuum sources. This is further supported by the frequent coincidence of outflows toward such sources, as discussed in Section 3.2. To determine whether the observed compact continuum sources are consistent with starless cores ($\sim 0.1 \ pc$) embedded within the mapped clumps ($\sim 1 \ pc$), in Section 4 we compare a subset of the observations to radiative transfer models of starless cores.

Some continuum sources without molecular line detections may be background galaxies. Deep surveys performed with ALMA (Hatsukade et al. 2013; Carniani et al. 2015) have determined source counts of background galaxies at 1.3 mm. The number of sources expected in the images with flux densities greater than $N(S_{1.3} > 0.3 \text{ mJy}) \lesssim 3$ over the 12 fields, measured as the HPBW area for each pointing, outside of which the degraded sensitivity yields negligible background sources. This represents approximately $\lesssim 5\%$ of the detected

Table 3ALMA Correlator Configuration

SPW	Cen. Freq. (GHz)	N	Bandwidth (kHz)	Bandwidth (km s ⁻¹)	Δf (kHz)	$\frac{\Delta v}{(\text{km s}^{-1})}$
1	216.112580	960	468750.0	650.252	488.28	0.677
2	217.104980	960	468750.0	647.280	488.28	0.674
3	218.222192	480	117187.2	160.991	244.14	0.335
4	218.475632	480	117187.2	160.804	244.14	0.335
5	218.760066	480	117187.2	160.595	244.14	0.335
6	219.560358	240	117187.2	160.010	488.28	0.667
7	230.538000	960	468750.0	609.564	488.28	0.635
8	231.321828	960	468750.0	607.499	488.28	0.632
9	233.820000	128	2000000.0	2564.301	15625.00	20.033

Note. Column descriptions: (1) Spectral window (SPW) ID number, (2) Center frequency of SPW in the rest frame, (3) Number of channels, (4), (5) SPW total bandwidth, (6), (7) SPW channel resolution. Uncertainties are given in parentheses.

Table 4
Spectral Line Transition Properties

Specie	Transition	Rest Freq. (GHz)	$\frac{E_{\mathrm{u}}/k}{\mathrm{(K)}}$	Ref.	SPW	$\Delta v \ (\text{km s}^{-1})$
DCO ⁺	3 → 2	216.1125800	20.74	(1)	1	0.68
c-HC ₃ H	$3_{3,0} \rightarrow 2_{2,1}$	216.2787560	19.47	(1)	1	0.68
SiO	$5 \rightarrow 4$	217.1049800	31.26	(1)	2	0.68
DCN	$3 \rightarrow 2$	217.2385378	20.85	(2)	2	0.68
p-H ₂ CO	$3_{0,3} \rightarrow 2_{0,2}$	218.2221920	20.96	(1)	3	0.34
p-H ₂ CO	$3_{2,2} \rightarrow 2_{2,1}$	218.4756320	68.09	(1)	4	0.34
CH ₃ OH	$4_{2,2} \rightarrow 3_{1,2}$	218.4400500	45.46	(1)	4	0.34
p-H ₂ CO	$3_{2,1} \rightarrow 2_{2,0}$	218.7600660	68.11	(1)	5	0.34
$C^{18}O$	$2 \rightarrow 1$	219.5603580	15.81	(1)	6	0.68
CO	$2 \rightarrow 1$	230.5380000	16.60	(1)	7	0.68
N_2D^+	$3 \rightarrow 2$	231.3218283	22.20	(2)	8	0.68

Note. Transition property reference key: (1) SLAIM, (2) CDMS.

sources, and thus does not have a significant effect on the calculation of the nearest neighbor separations or other estimated distributions of core properties.

3.2. CO and SiO Outflows

Ordered, bipolar molecular outflows driven by protostellar accretion provide a sensitive and unambiguous detection of embedded protostellar activity; see reviews by Arce et al. (2007) and Frank et al. (2014). In this section, we describe the properties of outflows detected with ALMA in CO $J=2 \rightarrow 1$ and SiO $J=5 \rightarrow 4$.

Outflows are identified through visual inspection of the CO data cubes in conjunction with the 1.3 mm maps overplotted. While the emission structures in the CO cubes are complex, bipolar outflows are clearly apparent as paired linear emission structures. These features are identified as linear features radiating from the same location, with highly ordered red and blue velocity components that are detected over many velocity channels (\gtrsim 10 km s⁻¹, \gtrsim 15 channels). Outflow candidate features with only a single red or blue component are also observed, but due to the greater ambiguity in identification, these are not regarded as clear signatures of star formation activity. The CO outflows are generally highly ordered in position and velocity, but spatial filtering of bright, extended

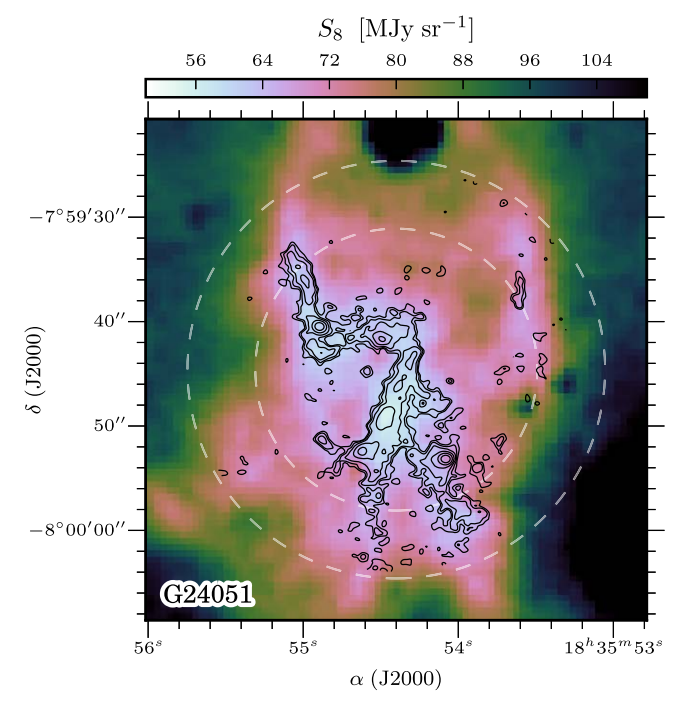


Figure 4. Comparison between the ALMA 230 GHz continuum (black lines) and IRAC 8 μm intensity S_8 (color map, inverted) for clump G24051. Good spatial correspondence is observed between the substructure in the ALMA continuum and the highest-extinction features in the GLIMPSE 8 μm map ($\theta_{\rm fwhm}\approx 2''$). The continuum images are shown without correction for primary beam attenuation, for visual display purposes, and the contours are at steps of 2, 3, 5, 10, 20, and 40 $\sigma_{\rm rms}$. The dotted lines show the 50% and 20% power points of the ALMA primary beam.

emission and self-absorption near the source systemic velocity complicate the identification of low-velocity ($|\nu| \lesssim 1.5~{\rm km~s^{-1}}$) outflow components. Higher-velocity components of the spectra also suffer both self-absorption from foreground CO clouds and confusion with bright Galactic emission, which can bias measurements of the maximum outflow velocity to lower values. Analysis of an example outflow in G24051 is presented in Appendix A.

We find that 9 out of 12 clumps are associated with bipolar CO outflows, and 16 outflows in total are observed. We also find that three out of 12 clumps are associated with bipolar SiO outflows, and four outflows in total are observed. The clumps

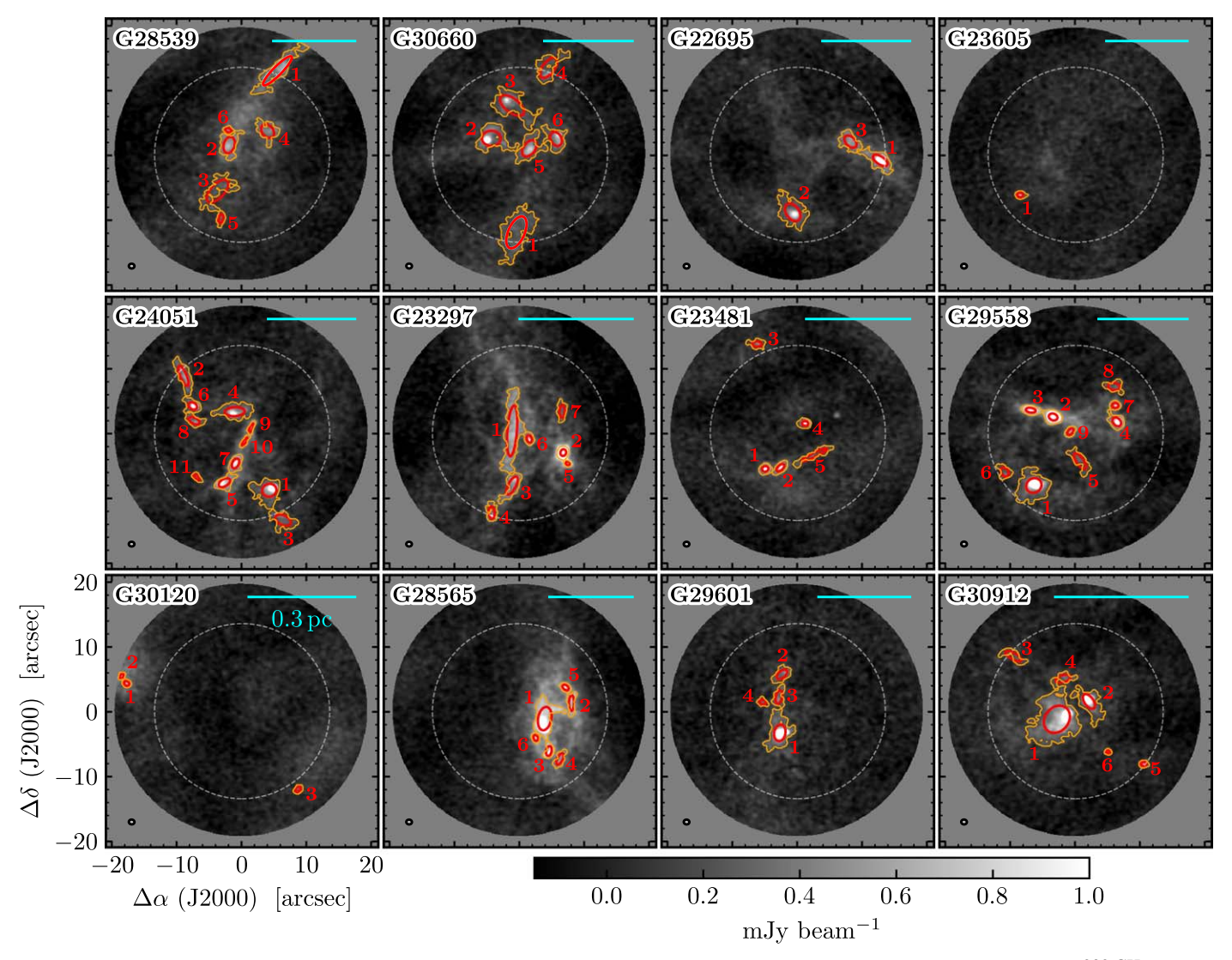


Figure 5. Dendrogram-extracted dense gas substructures (orange contour) overplotted onto the ALMA 12 + 7 m array jointly deconvolved 230 GHz line-free continuum images. Elliptical sources are visualized (red ellipses). Substructures are labeled by their catalog number from Table 5. The maps are uncorrected for primary beam attenuation, for visual display purposes. The color scale ranges from -0.15 to 1.0 mJy beam $^{-1}$ on a linear scaling. The scale bar (cyan) visualizes 0.3 pc at the clump heliocentric distance. The dashed circle shows the half-power beamwidth (27''), and the image extends down to the 20% power point (40'').

with outflows are reported in Table 6. Pairs of CO outflows originating from the same continuum source are also observed, as seen in G23297 S2 and G29601 S1, which point to unresolved protostellar multiple systems. Figure 7 presents the ALMA joint 12 + 7 m array CO $J = 2 \rightarrow 1$ integrated intensity maps for blue- and redshifted velocity components.

We also detect SiO emission toward several more continuum sources and positions without clear signs of ordered bipolar outflows. SiO emission detection is a strong indicator of protostellar activity, because of its origin in high-velocity shocks driven by protostellar outflows (Schilke et al. 1997). However, recent work has shown that low-velocity shocks (\lesssim 10 km s⁻¹) created by colliding flows may produce substantial distributed SiO emission (Jiménez-Serra et al. 2010; Nguyen-Lu'o'ng et al. 2013; Louvet et al. 2016). Thus, considered by itself, a detection of relatively narrow linewidth ($\Delta \nu \lesssim 10 \text{ km s}^{-1}$) SiO $J=5 \to 4$ emission is not an unambiguous indicator of star formation activity. Maps of SiO integrated intensities are presented in Appendix B.

3.3. Is G28539 a True Starless Clump?

The 70 μ m dark clump G28539 (upper left corner of Figures 3 and 7) shows no clear sign of CO or SiO outflows, and thus remains a starless clump candidate at the improved sensitivity of ALMA. Several indirect tracers of star formation are observed toward G28539, however, and we discuss these in turn.

Moderately high-excitation molecular lines ($E_u/K \gtrsim 50~K$) are unlikely to be excited in the cold 10 K gas expected to be found in starless cores and quiescent clump gas. Detection of such lines in our observations are thus indirect evidence of embedded protostars—although, as discussed in Section 3.2, it is possible that some of these lines are excited from low-velocity shocks originating from colliding flows. In G28539, a compact source of weak emission CH₃OH and H₂CO $3_{2,2} \rightarrow 2_{2,1}$ is detected. These features are not coincident with continuum emission and may originate from non-protostellar shocks, shocks of undetected protostellar outflows, or of embedded protostellar cores that are below our detection limit.

Table 5Core Observed Properties

Name	ID	α (ICRS)	δ (ICRS)	Ω_c	а	b	PA	$S_{ u}$	$\delta S_{ u}$	$S_{ u,\mathrm{pk}}$	СО	SiO
		(h:m:s)	(d:m:s)	$\Omega_{\rm c}$ (as ²)	(as)	(as)	(deg)	(mJy)	(mJy)	(mJy/bm)		
G22695	1	18:34:13.7336	-09:18:36.6910	9.30	2.597	1.213	146.0	17.284	0.109	6.414	1	
G22695	2	18:34:14.6345	-09:18:44.6915	16.54	3.022	1.976	126.1	9.083	0.196	1.518		
G22695	3	18:34:14.0405	-09:18:33.7904	7.17	2.256	1.444	135.6	5.348	0.133	0.737		
G23297	1	18:33:32.1419	-08:32:25.9306	22.70	7.853	1.461	85.5	16.431	0.309	0.727		
G23297	2	18:33:31.6164	-08:32:29.2777	2.79	1.055	0.870	72.4	11.515	0.088	6.381	2	
G23297	3	18:33:32.1439	-08:32:34.3684 -08:32:38.5247	6.86	3.124	1.180	61.9	5.699	0.130	0.925	1	
G23297 G23297	4 5	18:33:32.3527 18:33:31.5694	-08:32:38.3247 -08:32:30.9485	3.77 0.86	1.880 0.692	0.911 0.488	94.0 148.8	4.139 2.542	0.066 0.045	1.906 3.026	1	
G23297 G23297	6	18:33:31.9659	-08.32.30.9483 -08.32.27.1673	2.29	1.161	0.488	107.4	1.740	0.043	0.893		
G23297	7	18:33:31.6280	-08:32:22.9146	3.53	1.982	0.798	88.6	1.645	0.099	0.472		
G23481	1	18:35:59.8961	-08:39:08.0500	2.68	0.998	0.853	-164.0	3.514	0.085	2.311		
G23481	2	18:35:59.7404	-08:39:07.8724	3.04	1.464	0.758	-137.0	2.647	0.098	1.282	1	
G23481	3	18:35:59.9838	-08:38:48.7847	3.02	1.513	0.806	176.9	2.529	0.046	1.263		
G23481	4	18:35:59.4861	-08:39:01.0450	2.56	0.962	0.702	176.2	2.265	0.103	2.030		
G23481	5	18:35:59.3916	-08:39:05.8982	5.46	4.296	0.681	-153.8	1.920	0.142	0.385		
G23605	1	18:33:39.9726	-08:12:39.4169	1.88	0.938	0.651	177.4	1.371	0.058	1.197		
G24051	1	18:35:54.1219	-07:59:53.4130	13.49	2.213	1.980	-168.1	12.535	0.164	5.085		
G24051	2	18:35:55.0045	-07:59:35.7741	8.14	3.347	0.969	112.6	6.905	0.100	1.108		
G24051	3	18:35:53.9805	-07:59:58.0198	7.95	2.563	1.491	155.0	6.397	0.077	0.924		
G24051	4	18:35:54.4771	-07:59:41.2910	11.24	3.038	1.379	-176.6	5.844	0.207	1.192	1	
G24051	5	18:35:54.5839	-07:59:52.2422	4.87	1.920	1.103	-148.3	5.500	0.111	1.810	1	1
G24051	6	18:35:54.9096	-07:59:40.4092	4.36	1.417	1.011	150.3	3.820	0.100	2.154		1
G24051 G24051	7 8	18:35:54.4693 18:35:54.8945	-07:59:49.2862 -07:59:42.6850	4.14 3.87	1.641 1.813	0.987 0.959	62.3 154.2	3.810 1.911	0.120 0.102	1.044 0.612		
G24051	9	18:35:54.3071	-07.59.42.0830 -07:59:43.7882	1.42	1.354	0.939	68.1	1.057	0.102	0.612		
G24051	10	18:35:54.3750	-07:59:45.8972	1.44	1.396	0.454	55.4	1.037	0.077	0.645		
G24051	11	18:35:54.8697	-07:59:51.3991	1.47	1.060	0.555	135.5	0.659	0.054	0.506		
G28539	1	18:44:22.2420	-04:01:44.7142	16.35	6.175	1.334	45.3	19.114	0.121	1.842		
G28539	2	18:44:22.7348	-04:01:56.1668	8.58	2.585	1.671	73.6	5.411	0.183	0.711		
G28539	3	18:44:22.8536	-04:02:03.2640	12.63	4.346	2.086	46.9	4.587	0.191	0.439		
G28539	4	18:44:22.3397	-04:01:54.0246	7.39	2.372	1.682	130.3	4.055	0.156	0.603		
G28539	5	18:44:22.8195	-04:02:07.5292	2.36	1.403	0.682	80.2	1.249	0.064	0.526		
G28539	6	18:44:22.7434	-04:01:53.8880	1.41	0.930	0.656	169.0	0.842	0.070	0.551		
G28565	1	18:44:17.2674	-04:02:03.5257	14.00	3.641	2.023	79.3	17.943	0.226	2.499	1	1
G28565	2	18:44:16.9912	-04:02:01.1285	3.52	2.395	0.776	89.0	3.894	0.093	0.946		
G28565 G28565	3 4	18:44:17.2241 18:44:17.1101	-04:02:08.5328 -04:02:09.7546	2.60 3.33	1.532 1.914	0.830 0.810	78.1 62.9	3.604 3.087	0.083 0.082	1.443 0.827		
G28565	5	18:44:17.0529	-04.02.09.7340 -04:01:58.7236	1.87	1.082	0.690	143.2	2.401	0.062	1.347		
G28565	6	18:44:17.3596	-04.01.36.7230 -04:02:06.5025	1.47	0.935	0.670	109.7	1.561	0.007	0.903		
G29558	1	18:44:37.5015	-02:55:12.4812	20.09	2.432	2.174	-146.5	20.697	0.184	6.613		
G29558	2	18:44:37.3029	-02:55:01.9117	4.83	1.372	1.029	161.9	10.569	0.130	4.941	1	
G29558	3	18:44:37.5338	-02:55:00.8673	3.41	1.524	0.742	171.2	6.624	0.093	3.588	1	
G29558	4	18:44:36.6483	-02:55:02.6587	4.40	1.548	1.109	134.4	4.624	0.114	1.666		
G29558	5	18:44:37.0267	-02:55:08.7202	6.09	2.893	1.085	125.8	1.881	0.146	0.332		
G29558	6	18:44:37.8020	-02:55:10.4118	3.46	1.516	1.090	125.5	1.810	0.065	0.681		
G29558	7	18:44:36.6640	-02:55:00.1446	1.87	0.937	0.766	176.3	1.688	0.070	1.116		
G29558	8	18:44:36.6775	-02:54:57.2062	3.91	1.871	1.128	171.4	1.626	0.090	0.472		
G29558	9	18:44:37.1252	-02:55:04.1785	2.00	1.141	0.739	45.8	1.357	0.090	0.584		
G29601	1	18:47:25.3865	-03:13:29.3698	16.05	2.547	1.728	79.6	15.771	0.240	6.686	2	1
G29601	2	18:47:25.3644	-03:13:20.3497	4.94	1.908	1.077	-140.3	2.192	0.123	0.567		
G29601	3	18:47:25.3951	-03:13:23.8223	4.15	2.104	0.976	78.6	1.751	0.124	0.501		
G29601	4	18:47:25.5623	-03:13:24.6212	1.69	0.999	0.716	151.3	0.541	0.074	0.341		
G30120	1	18:50:24.7282	-03:01:27.2884	1.38	0.820	0.683	147.5	3.924	0.020	2.709	1	
G30120 G30120	2 3	18:50:24.7785 18:50:22.9654	-03:01:26.1411 -03:01:43.6061	0.93 1.61	0.737 0.912	0.548 0.680	53.8 -137.5	2.868 1.232	0.014 0.034	2.807 0.854		
G30660	1	18:47:07.7985	-02:00:24.1287	27.58	5.270	2.513	66.2	15.430	0.191	0.902		
G30660	2	18:47:08.0553	-02:00:09.6124	14.88	2.912	2.347	178.5	8.489	0.224	2.140		

	Table	5
((Continu	ied)

Name	ID	α (ICRS) (h:m:s)	δ (ICRS) (d:m:s)	$\frac{\Omega_{\varsigma}}{(as^2)}$	a (as)	b (as)	PA (deg)	S_{ν} (mJy)	δS_{ν} (mJy)	$S_{\nu,pk}$ (mJy/bm)	СО	SiO
G30660	3	18:47:07.8433	-02:00:04.5482	18.40	4.397	2.139	142.3	8.257	0.219	1.318		
G30660	4	18:47:07.4677	-01:59:58.7398	11.09	3.618	1.832	52.6	7.588	0.095	0.984		
G30660	5	18:47:07.6647	-02:00:11.1585	11.19	2.859	1.779	53.0	5.183	0.210	0.812		
G30660	6	18:47:07.3910	-02:00:09.7055	8.59	2.296	1.622	119.3	4.896	0.162	1.128		
G30912	1	18:45:11.4745	-01:28:04.9508	44.25	4.523	3.651	51.0	27.344	0.403	2.728	1	
G30912	2	18:45:11.1447	-01:28:02.2048	12.95	2.595	1.372	124.9	9.536	0.224	4.324	2	
G30912	3	18:45:11.9211	-01:27:55.2127	4.29	2.778	0.976	151.1	2.249	0.069	0.682		
G30912	4	18:45:11.4095	-01:27:58.6881	4.05	2.365	1.096	-161.7	1.498	0.114	0.430		
G30912	5	18:45:10.5824	-01:28:11.8467	1.53	0.820	0.629	179.5	1.399	0.039	1.353		
G30912	6	18:45:10.9468	-01:28:09.9788	0.83	0.600	0.516	168.0	0.360	0.045	0.518		

Note. Column descriptions: (1) Target clump name, (2) substructure ID number, (3) centroid R.A. coordinate, (4) centroid decl. coordinate, (5) total dendrogram area, (6) Gaussian major FWHM, (7) Gaussian minor FWHM, (8) Gaussian position angle, (9) source integrated 1.3 mm flux density, (10) uncertainty in source integrated flux density, (11) source peak flux density, (12) number of bipolar CO outflows, (13) number of bipolar SiO outflows.

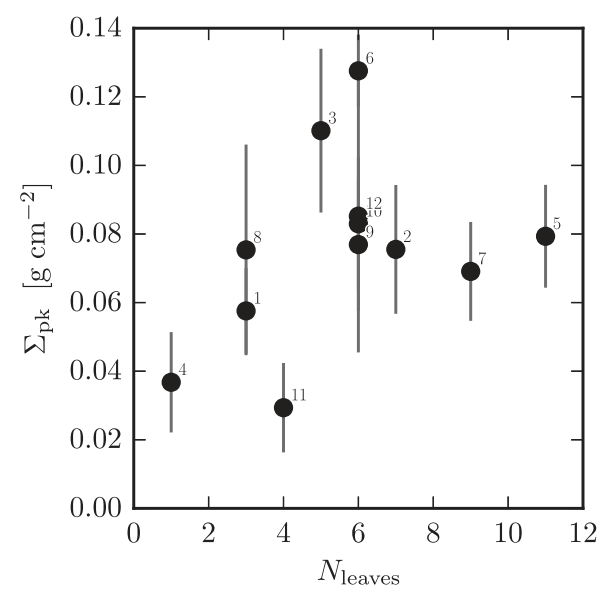


Figure 6. Peak clump mass surface density from the BGPS 1.1 mm data vs. the number of leaves (i.e., dendrogram leaves) per clump from the ALMA observations. The data hints at an increasing trend of higher-mass surface density clumps associated with a higher degree of fragmentation.

Similarly, a compact source of SiO is also detected and does not coincide with any continuum emission feature (it may be seen on the west side of the field in Figure 15).

There exist weak 24 μm sources in the vicinity of the clump boundaries as defined by the 350 μm and 500 μm emission, notably including a faint source within the extinction feature \sim 1' east of the ALMA field (see 24 μm panel in Figure 1), a brighter source on the southeastern outskirt of the clump, and a marginal feature coincident with the continuum source in the NW edge of the ALMA field of view. Because of the substantial contamination from evolved stars, 24 μm emission alone is not a robust indicator of protostellar activity. If these sources are indeed protostars associated with the clump, then they would be evidence that star formation has begun in G28539.

Deep radio continuum observations, when available, also provide a diagnostic of star formation activity, because they are sensitive to the ionized gas in ultra- and hypercompact H II regions, ionized winds, and jets from low- to intermediate-mass

protostars. Rosero et al. (2016) carried out deep JVLA C and K band observations toward a sample of high-mass clumps that contains source G28539 in the field "G28.53-00.25." The HPBW of the primary beam for the JVLA at C band is 9'.2 at 4.2 GHz (LSB) and 4.2 at 7.4 GHz (USB), with synthesized HPBW resolution of approximately ~ 0.4 in the A configuration. Using the radio continuum to bolometric luminosity scaling relations for protostars as given in Equation (3) of Shirley et al. (2007), the measured $\sigma_{\rm rms} = 3~\mu \rm Jy~beam^{-1}$ sensitivity at $d_{\odot} = 4.7 \,\mathrm{kpc}$ can be converted to a 1σ bolometric luminosity sensitivity of $\sim 30 L_{\odot}$, which is reasonably comparable to the PACS 70 μ m sensitivity from Hi-GAL. Here, a faint point source is detected near the center of the ALMA pointing, detected in both sidebands at moderate significance (8 and 5σ in LSB and USB, respectively). The measured in-band spectral index ($S \propto \nu^+ \alpha$) $\alpha = -0.65 \pm 0.46$ favors a nonthermal synchrotron-dominated source, but the weak constraint is consistent with thermal free–free emission $\alpha = -0.1$ at $1.2\sigma_{\rm rms}$. The location $18^{\circ}44'22''621-4^{\rm h}02^{\rm m}00^{\rm s}380$ (J2000) is not coincident with millimeter continuum or spectral line emission in the ALMA data. Given the lack of a clear association, we conclude that this radio continuum source is likely an extragalactic contaminant and not an indicator of protostellar activity.

In summary, indirect evidence for star formation exists from two different tracers: (1) 24 μ m sources at the edge or outside of the ALMA field of view, and (2) ALMA detections of CH₃OH and SiO that are not clearly associated with continuum sources. G28539 is the most massive clump in the sample ($M_{\rm cl} \approx 3600 \, M_{\odot}$) and shows fairly limited signs of fragmentation. After the ALMA observations, G28539 is the only starless clump candidate remaining in our sample. It is thus a target of great interest for studying the initial conditions of high-mass star formation.

4. Modeling Continuum Sources

4.1. Starless Core Models

A diverse range of continuum substructures are found to be present in SCCs, including unresolved compact sources, filaments, and extended emission with lower surface brightness. In this section, we analyze whether cores with bright, unresolved continuum emission on scales <1500 au $(\sim \theta_{\rm syn}/2)$

Table 6
Band 6 Detections^a

Name	Cont.	ont. Deuteration		Kin	Kinematic		High-excitation				Outflow	
	1.3 mm	DCO ⁺	DCN	N_2D^+	C18O	H ₂ CO ^b	H ₂ CO	H ₂ CO	c-C ₃ H ₂	CH ₃ OH	СО	SiO
G28539	D	W	W	N	D	D	N	W	N	W	D	D
G30660	D	D	N	N	D	D	W	W	D	D	D	D
G22695	D	W	W	N	D	D	D	D	N	D	В	D
G23605	D	N	N	N	D	D	N	W	N	W	D	N
G24051	D	D	D	D	D	D	D	W	D	D	В	В
G23297	D	D	D	W	D	D	D	D	W	D	В	D
G23481	D	N	N	N	D	D	D	D	N	D	В	W
G29558	D	D	W	D	D	D	D	D	D	D	В	D
G30120	W	N	N	N	D	W	N	N	N	W	В	D
G28565	D	D	W	D	D	D	D	D	D	D	В	В
G29601	D	D	W	N	D	D	D	D	W	D	В	В
G30912	D	D	D	W	D	D	D	D	W	D	В	D

Notes.

are necessarily protostellar even without detections of outflows or strong high-excitation molecular lines. We also model whether low- to intermediate-mass starless cores are accurately recovered in the observations, and we perform detailed modeling of high-mass starless core candidates in clump G28539.

To characterize the continuum features in our images, we apply the radiative transfer code RADMC-3D (Dullemond et al. 2012) to self-consistently calculate the equilibrium dust temperature distributions of externally heated starless cores and to produce synthetic images. We follow an approach to modeling starless cores similar to that found in Shirley et al. (2005) and Lippok et al. (2016). We apply conventional assumptions for the dust properties (Ossenkopf & Henning 1994; Weingartner & Draine 2001; Young & Evans 2005) and interstellar radiation field (ISRF, Draine 1978; Black 1994). A detailed description of the computed models may be found in Appendix C.

We apply a spherically symmetric Plummer-like function to parameterize the model radial density profile (Plummer 1911; Whitworth & Ward-Thompson 2001; Lippok et al. 2016). The gas density profile $n_{\rm H}$ can be expressed as:

$$n_{\rm H}(r) = (n_{\rm in} - n_{\rm out}) \left[1 + \left(\frac{r}{R_{\rm flat}} \right)^2 \right]^{-\eta/2} + n_{\rm out}$$
 (1)

for radius r, inner gas density $n_{\rm in}$, outer gas density $n_{\rm out}$, flat radius $R_{\rm flat}$, and power law exponent η (n.b., an isothermal Bonnor–Ebert sphere may be approximate with $\eta=2$; see Ebert (1955) and Bonnor (1956)). The strength of the interstellar radiation field (ISRF) is varied from the local value by a multiplicative scale factor $s_{\rm isrf}$. We compute 10^4 models, randomly sampling the parameter space by drawing values from a uniform distribution in log-space within the ranges for the parameters $n_{\rm in}=1\times 10^4$ – 1×10^7 cm⁻³, $n_{\rm out}=1\times 10^1$ – 1×10^3 cm⁻³, $R_{\rm flat}=1\times 10^3$ – 2×10^4 au, and $s_{\rm isrf}=1$ –100, while $\eta=2.5$ –5.5 is drawn uniformly in linear space. Models are evaluated on a logarithmic radial grid from 2.5×10^2 au to 6.0×10^4 au. These values are chosen to cover the range of values from the sample of low- and

intermediate-mass cores in Lippok et al. (2016), but extended to higher $n_{\rm in}$ and smaller $R_{\rm flat}$. After computing the radiative transfer, the models are ray-traced by RADMC-3D and projected to a fiducial distance of $d_{\odot}=4$ kpc.

4.2. Model Recovery

We find that 53% of the computed models $(5268/10^4)$ meet the detection threshold of $S_{1.3 \text{ mm,pk}} > 5\sigma_{\rm rms}$ when convolved with a $\theta = 0.$ "8 Gaussian beam. The cut in peak flux density has no effect on the recovered distributions of η and $n_{\rm out}$, and minimal effects on $R_{\rm flat}$ and $s_{\rm isrf}$, with an increase in the median values by a factor of 1.5 and 1.2, respectively, over the distribution of model cores.

It is important to keep in mind that the suite of model cores is constructed to span the parameter space of relevant values, not to represent an observed or predicted core mass function. We do not use the fractions of detectable cores to infer completeness, but rather to show the expected range of physical parameters for which cores can be recovered. To estimate this, we sort the models by M and s_{isrf} , counting both the fraction of detectable cores and the regions of parameter space with at least one detectable model (Figure 8). Computing the detection fraction in this way has the effect of marginalizing over our uncertainty in R_{flat} , η , n_{in} , and n_{out} , which are poorly constrained with our single-wavelength maps. Figure 8 (left) shows that, at 50% completeness, the cores at $s_{isrf} \sim 3$ are recovered for $M \gtrsim 4~M_{\odot}$, and this extends down to $M \sim 1~M_{\odot}$ for the extreme value $s_{isrf} = 100$. However, Figure 8 (right) shows that it is possible to recover lower-mass cores if the ranges of models is restricted to those that are the most compact (where $R_{\rm flat} < 3 \times 10^3 \, {\rm au}$, $\eta > 4.5$) and have high central densities ($n_{\rm in} > 1 \times 10^5 \, {\rm cm}^{-3}$). For these compact sources, $M \sim 1 M_{\odot}$ models may be recovered at $s_{\rm isrf} \sim 3$, and down to $M \sim 0.2 M_{\odot}$ for $s_{isrf} = 100$.

From these models, we can infer that the completeness expected from our point-source sensitivity, $\sim 0.3~M_{\odot}$ at $6\sigma_{\rm rms}$, is an underestimate if the majority of cores are resolved; see also Appendix A in Beuther et al. (2018). Low-mass cores with extended profiles will thus go undetected with a criterion based

^a Detection flags: D represents detection with $S/N \geqslant 7\sigma$, W weak detection with $5\sigma \leqslant S/N < 7\sigma$, N nondetection with $S/N < 5\sigma$, and B detection of bipolar outflow.

^b H_2CO transitions listed in order of $3_{0,3} - 2_{0,2}$, $3_{2,1} - 2_{2,0}$, and $3_{2,2} - 2_{2,1}$.

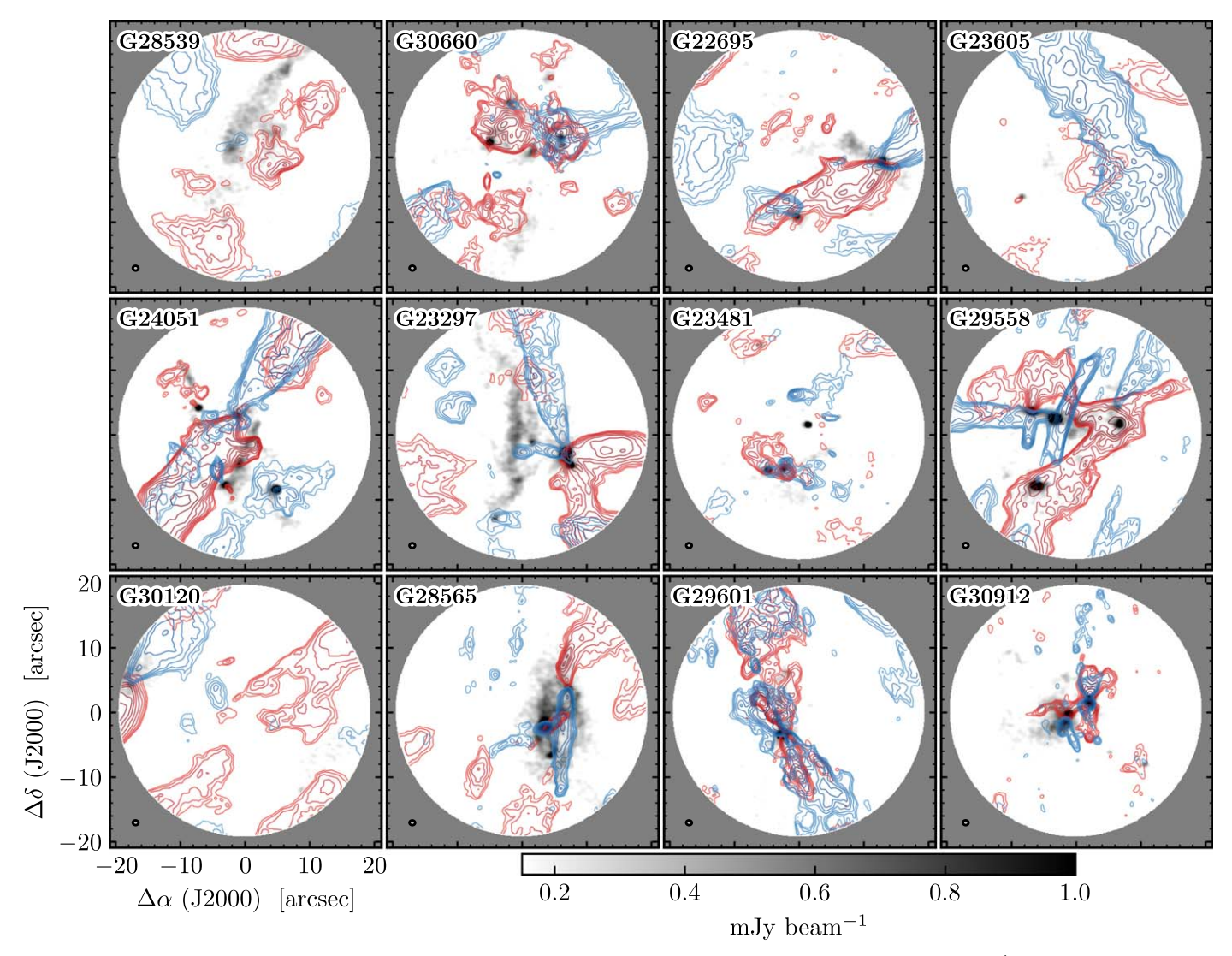


Figure 7. ALMA joint 12 + 7 m array CO $J = 2 \rightarrow 1$ intensity of velocity components integrated between offsets 5 and 15 km s⁻¹ (red contours) and between offsets -5 and -15 km s⁻¹ (blue contours). Bipolar outflows are observed toward 9/12 clumps. Contours are shown at logarithmically spaced steps of 0.16, 0.22, 0.29, 0.40, 0.54, 0.74, 1.00, 1.36, 1.85, and 2:6 Jy km s⁻¹. The inverted grayscale image shows the 230 GHz continuum. The image extends down to the 20% power point (40''). The maps are made from the dirty image cubes and have not been deconvolved with CLEAN.

on peak intensity, leading to our seemingly shallow limit of $\sim 1-4~M_{\odot}$. Observationally, we must approach extended emission at low S/N with caution because there is extended structure in the maps on scales larger than the 12 m primary beam that cannot be adequately CLEANed. For this reason, we do not attempt to identify or catalog sources down to the limits of statistical significance for extended and spatially integrated flux densities; instead, we maintain a conservative detection limit based on source peak flux density. The typical integrated flux density of a source is $S_{1.1} \sim 1-10~\text{mJy}~(M \sim 1-10~M_{\odot}, \text{assuming}~T_{\rm d}=12~\text{K}~\text{and}~d_{\odot}=4~\text{kpc}),$ and generally consistent with the thermal Jeans mass $M_{\rm j,th}$ for a uniform medium at the density of the clump, $M_{\rm j,th}\sim 2~M_{\odot}$, where $M_{\rm j,th}\equiv (4\pi/3)(\lambda_{\rm j,th}/2)^3\rho_0$ for thermal Jeans length $\lambda_{\rm j,th}$ and average density ρ_0 (McKee & Ostriker 2007); see Section 5 for an analysis of the Jeans length $\lambda_{\rm j,th}$.

4.3. Synthetic Observations with CASA

We now investigate whether the models of starless cores provide adequate fits to the brightness profiles present in the

SCCs of this survey. We find that compact sources of continuum emission that are unresolved (i.e., deconvolved sizes $\lesssim 1500$ au, $\approx \theta_{\rm syn}/2$) are poorly fit by models of starless cores. Without multiple wavelength observations or gas kinetic temperature information, the radial dust temperature profiles of the cores are poorly constrained. Because of the substantial systematic uncertainties presented in single-wavelength observations and potentially undetected embedded protostars, we do not perform a fit to every continuum source, but instead select a few characteristic examples for quantitative comparison. We create synthetic observations from the models using the CASA sm module by predicting onto the observed visibilities (gridded beforehand for computational efficiency) and imaged without noise using the same tclean configuration as the observations. This does not introduce a significant effect on the models, however, because nearly all the flux is concentrated on radii $r < 2 \times 10^4$ au or angular diameters of $\lesssim 8''$, appreciably less than half of the 12 m array 27" HPBW and substantially less than the maximum recoverable scale of 33" from the 7 m array. A subset of models were further tested for consistency. Because the aim of this comparison is to achieve an

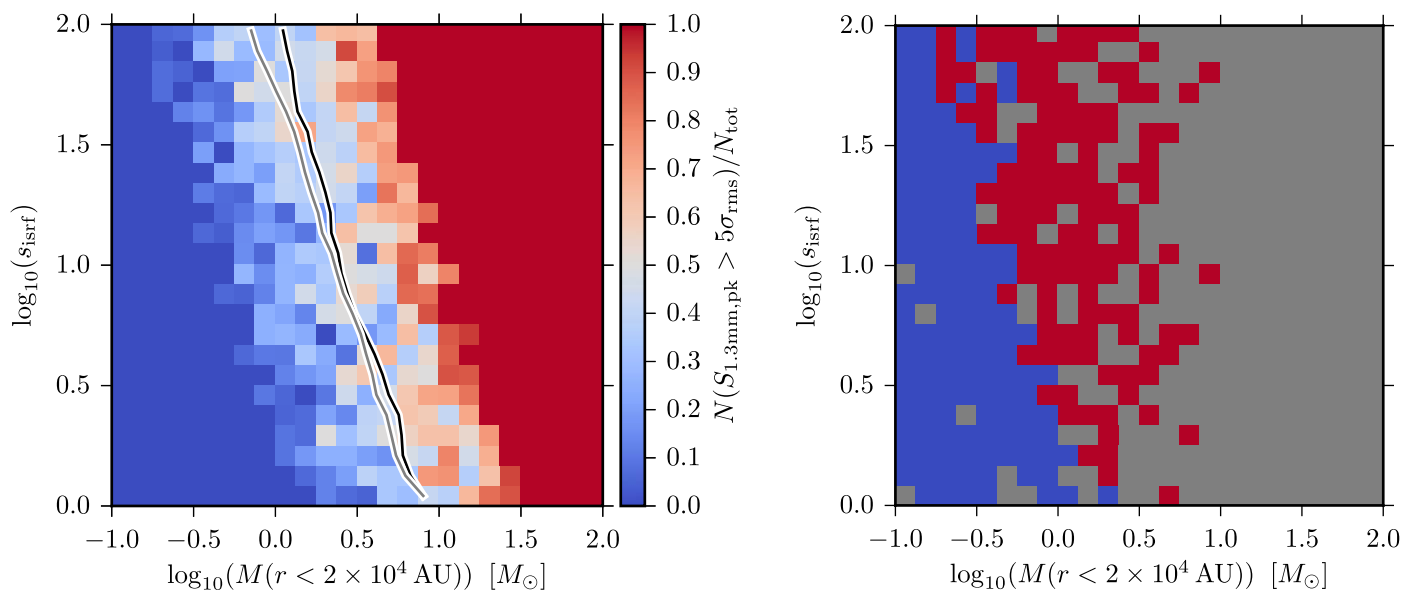


Figure 8. Left: fraction of the computed models with peak flux densities $S_{1.3 \text{ mm,pk}}$ meeting the source detection criteria $>5\sigma_{rms}$ in the images as a function of $M(r < 2 \times 10^4 \text{ au})$ and s_{isrf} . Lower-mass cores meet the criteria for larger values of s_{isrf} . The 50% detection threshold for all models (black line) and 50% detection threshold for models with $n_{in} > 10^5 \text{ cm}^{-3}$ (gray line) are shown. Cores in this range with $M \sim 1$ -6 lie above this threshold, depending on s_{isrf} , and are relatively insensitive to the choice of model parameters. Note that, for $\log_{10}(s_{isrf}) \sim 0.5$ (or $s_{isrf} \sim 3$), the distribution above $M \gtrsim 4 M_{\odot}$ meets the detection criteria. Right: detection criteria for "compact" models ($R_{flat} < 3 \times 10^3 \text{ au}$, $\eta > 4.5$) with high central densities ($n_{in} > 10^5 \text{ cm}^{-3}$), for cases where any model meets the criteria (red) and for cases where none do (blue). Compact starless core models with $M \sim 1 M_{\odot}$ are detectable at $s_{isrf} \sim 3$. Regions that are not sampled by the compact subset of models are shown in gray. Note that, because the maximum $n_{in} = 10^7 \text{ cm}^{-3}$, models with $M \gtrsim 10 M_{\odot}$ are more extended.

understanding of a few representative sources, rather than to construct a detailed parameter estimation, we do not image the full suite of models. Instead, we convolve the models with the angular size of the synthesized beam ($\theta_{\rm syn}=0.^{\prime\prime}.8$) and convert to radial brightness profiles.

4.4. Comparison to Observations

We compare the observations and models using a method based on the χ^2 statistic, where the reduced $\chi^2_{\rm r}$ may be expressed as

$$\chi_{\rm r}^2 = \frac{1}{\nu} \sum_i \frac{(o_i - m_i)^2}{\sigma^2}$$
 (2)

for degrees of freedom ν , independent measurements i, measurements o_i , model values m_i , and variances σ^2 . We discriminate between models based on the goodness-of-fit metric $\Delta\chi^2_{\rm r} \equiv \chi^2_{\rm r} - \chi^2_{\rm r,best}$ from Robitaille et al. (2007) and Robitaille (2017). Robitaille et al. apply the heuristic that models with $\Delta\chi^2_{\rm r} < 3$ are considered good fits and all others are rejected as poor fits. Robitaille et al. further note that the Bayesian likelihood under the assumption of normal errors (i.e., $P(D|\theta_j, M) \propto \exp{[-\chi^2/2]}$ for data D, parameters θ_j , and model M) yields too stringent a definition of probability, given the systematic sources of error in the measurements and the poor physical correspondence of the model to nature. This ultimately provides a more conservative criteria for rejecting poor fits, as the $\Delta\chi^2_{\rm r}$ heuristic likely overestimates uncertainties.

We consider two example starless core candidates, G28539 S2 and S4 (see Figure 5 and Table 5), because they: (1) lack unresolved continuum emission at their center, (2) host no outflows or other indicators of star formation activity, and (3) are relatively isolated such that radial brightness profiles can be adequately extracted. G28539 S2 and S4 are also of interest

because they are among the brightest such sources, and thus are good high-mass starless core candidates.

We extract radial brightness profiles for the cores by extracting the integrated flux density within 0."2 diameter annuli about the central position. Uncertainties in the integrated flux densities are calculated as the $\delta S_{\nu} = \sigma_{\rm rms} \sqrt{\Omega_{\rm ann}/\Omega_{\rm bm}}$ for the solid angle of the annulus $\Omega_{\rm ann}$ and the synthesized beam solid angle $\Omega_{\rm bm}$. The radial brightness profiles of the models are then compared by Equation (2) for degrees of freedom $\nu = r_{\text{max}}/0.^{"}2-5 \approx 15$ (maximum radius $r_{\text{max}} = 3.^{"}5-4.^{"}0$). Well-fit models are then selected where $\Delta \chi_{\rm r}^2 < 3$. Figure 9 shows the best-fit models compared to the observations, and Figure 10 shows the radial brightness profiles with the range of fits. We find that the extended brightness profiles are fit well by the starless core models ($\chi^2_{\rm r,best}=1.1$ and 0.12 for S2 and S4 respectively). If the range of models are limited to those that resulted in $T_d(r = 1 \times 10^3 \text{ au}) = 7-13 \text{ K}$, in order to be broadly consistent with the clump average temperature derived from the Hi-GAL SED and GBT NH3 fits (see also the detailed considerations in Tan et al. (2013)), then $M_{\rm S2}=29^{52}_{15}\,M_{\odot}$ and $M_{\rm S4} = 14_{6.0}^{34} \, M_{\odot}$, for the median, maximum, and minimum model mass. With a core star formation efficiency of 30%, it is possible that these cores may form high-mass stars $(M_* > 8 M_{\odot})$. Assuming a 50% formation efficiency from models regulated by outflows (Zhang et al. 2014), the maximum expected stellar mass for S2 could be $M_* \approx 26 M_{\odot}$. Given the fact that these cores are not associated with outflows in the ALMA data or other high-excitation molecular lines, they are excellent candidates for high-mass starless cores.

G29558 S1 represents the class of compact continuum sources in our data set. Analysis of this source is then a test of whether the compact sources are described well by starless core models—or alternatively, likely to host embedded protostars. This continuum source has some surrounding extended continuum emission and does not show clear outflows traced

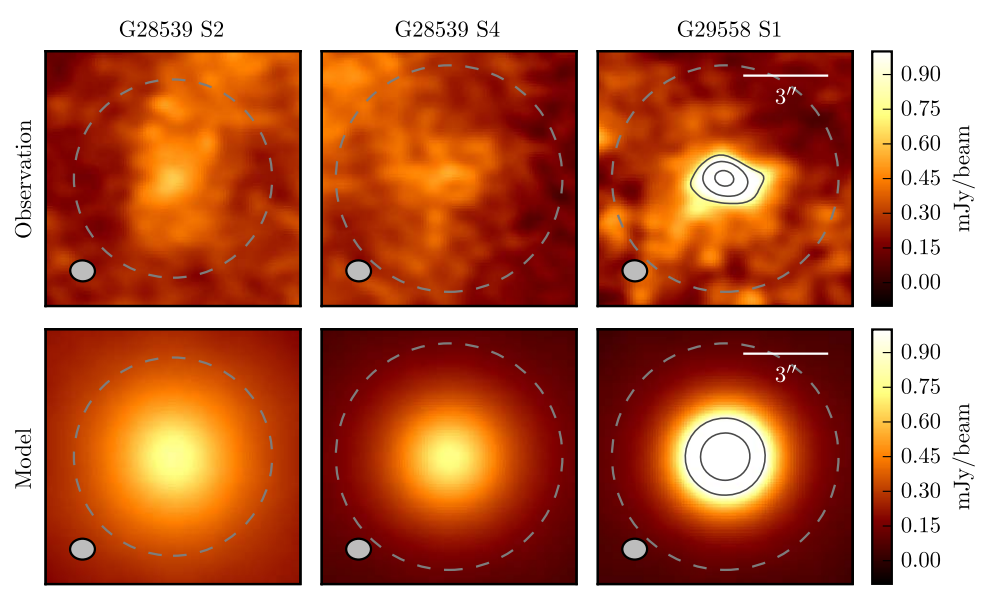


Figure 9. Top row: 230 GHz continuum images of example sources G28539 S2, G28539 S4, and G29558 S1. Contours (black solid) show 10, 20, and $50\sigma_{rms}$, and the 3."5 and 4" radius apertures (gray dashed) show the region over which the radial brightness profiles used for the model comparison were extracted. The beam ($\theta_{syn} \sim 0$."8), scale bar (3"), and color bar (-0.1 to 1 mJy beam $^{-1}$) are also visualized. Bottom row: best-fit models when run through the CASA simulator (bottom row, same color scale as above). The models for the resolved sources G28539 S2 and S4 are fit well by models of starless cores ($\chi_r^2 \sim 0.1$ –1), while the unresolved source G29558 S1 is poorly fit ($\chi_r^2 > 20$).

by CO or SiO, but it is associated with weak CH₃OH and p-H₂CO emission. It is bright with peak flux density 6.6 mJy and is similar to other continuum sources with associated outflows. We find that the models fit the observations poorly, with $\chi^2_{\rm r,best} = 23.9$ and no models for $\Delta\chi^2_{\rm r} < 9$. The properties are pushed to the extremes of parameter space: $s_{\rm isrf} \sim 100$, $\eta \sim 5.5$, and $n_{\rm in} \gtrsim 1 \times 10^7 \, {\rm cm}^{-3}$. The moderate $R_{\rm flat} \sim 5 \times 10^{-3}$ 10³ au is a compromise between the compact and extended components of the brightness profile. The poor model fits to G29558 S1 do not strictly require that it or any other individual source is protostellar (models with $n_{\rm in} \gtrsim 10^8 \, {\rm cm}^{-3}$ and $R_{\rm flat} < 10^3 \, {\rm au}$ would likely fit the observations). However, such extreme starless cores are unlikely to be observed in significant numbers in our sample, where ~40% of fragments are compact continuum sources. The freefall timescale of a core with $n_{\rm in}=10^8\,{\rm cm}^{-3}$ would be $t_{\rm ff}\approx 3\times 10^3\,{\rm yr}$, and for $n_{\rm in}=10^7\,{\rm cm}^{-3}$ would be $t_{\rm ff}\approx 1\times 10^4\,{\rm yr}$. These are shorter than the inferred ages from the extent and velocity of the observed outflows, although these have substantial uncertainties. Together, the observed properties of these compact continuum sources are more favorably explained as embedded low- to intermediate-mass YSOs, which at \sim 4 kpc would be both of comparable brightness and unresolved (see Section 3.1). A detailed analysis of the starless and protostellar core properties and dynamics will follow in a future work incorporating NH₃ data from the VLA observations.

5. Fragmentation Scale

5.1. Nearest Neighbor Separations and Monte Carlo Simulations

We characterize the linear fragmentation scale in terms of the nearest neighbor separation δ'_{nns} between dendrogram leaves in each clump. Geometric projection of sources in the plane of the sky will systematically decrease δ'_{nns} from the true value, δ_{nns} . In this work, we employ Monte Carlo random sampling to

deproject δ'_{nns} statistically. Thus, while the uncertainty in δ_{nns} may make constraints for any individual pair of sources quite weak, with prior assumptions on the relative positions of sources, the posterior distribution from the ensemble of all δ_{nns} measurements in our sample of SCCs can be readily constrained.

Monte Carlo sampling is used to draw realizations of relative line-of-sight distances z, computing δ_{nns} for each source from the Cartesian coordinates (x, y, z). We use the hierarchical classification of sources in the dendrogram to discriminate between two methods of drawing z values: (i) isolated sources, and (ii) sources with common surrounding emission. If sources are isolated (Case i), forming a tree with a single branch, then for each trial, we draw line-of-sight distances from a Gaussian distribution with standard deviation $\sigma_z = 0.15 \text{ pc}$ (FWHM 0.35 pc), chosen such that the double-sided $2\sigma_z$ interval is 0.6 pc, which is the approximate diameter inferred from the $8 \mu m$ maps (see Figures 1 and 4). If sources are associated within the same branch of the dendrogram (Case ii; i.e., they are within a common base isocontour of emission), then we assume that those sources are connected in a filamentary gas structure with unknown inclination with respect to the observer. For each trial, we draw a common inclination ϕ for the group, pivoting along the major axis, with the pivot axis fixed to z = 0 at the projected geometric center. Inclinations are drawn such that the length between the two components with the maximum separation $\delta_{
m max}$ is less than D=0.6 pc, and thus ϕ is drawn uniformly within the interval $(-\arccos(\delta_{\max}/D), +\arccos(\delta_{\max}/D))$. If $\delta_{\max} > D$, then ϕ is drawn uniformly within $(-65^{\circ}, +65^{\circ})$, such that $\delta_{\max} \lesssim 1.4$ pc to extend out to a typical clump effective radius of $R \approx 0.7$ pc. In total, there are 17 (26%) isolated sources and 49 (74%) grouped sources. Without more detailed knowledge available, informed from either additional observational data or theoretical simulations, we consider this scheme a conservative way to correct the data for geometric projection. While the

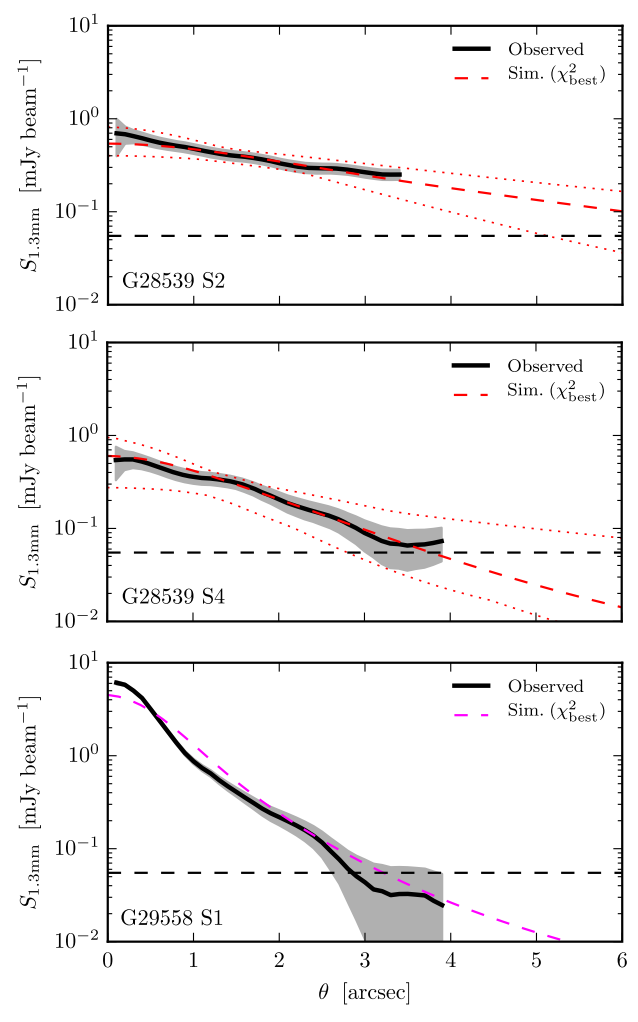


Figure 10. Example ALMA observed sources fit with the suite of starless core models. The observed radial brightness profiles (black) and the image $1\sigma_{\rm rms}$ (gray region) are shown with the best-fit model (red dashed) and envelope of all models that satisfy $\chi^2_{\rm r}-\chi^2_{\rm r,best}<3$ (red dotted). The error envelope is calculated as the $\pm 1\sigma$ uncertainty of the integrated intensity within the annular aperture at the angular radius θ . The profiles are truncated to where the source is mostly symmetric. The map rms is visualized (gray dashed line). Top: $\chi^2_{\rm r,best}=1.1.$ Middle: $\chi^2_{\rm r,best}=0.12.$ Bottom: $\chi^2_{\rm r,best}=23.9$ (magenta dashed), with no models for $\chi^2_{\rm r}-\chi^2_{\rm r,best}<9.$ The resolved sources G28539 S2 and S4 are fit well by starless core models, while the models fail to fit the high-S/N, unresolved inner component in G29558 S1.

assumptions in the correction are simple and imperfect, for brevity, we refer to the distributions of MC trials as "projection-corrected" below in order to distinguish them from the projected data. Extensions of this method may opt to use more sophisticated schemes to group sources beyond common millimeter continuum emission, such as grouping sources through a lower-density kinematic tracer or a source-density-based clustering algorithm.

With no correction applied, the distribution of projected separations has a median value of $\mu_{1/2}(\delta'_{nns})=0.083$ pc, with a (16, 84) percentile interval of (0.051, 0.140) pc. To calculate the projection-corrected separations, we compute 1×10^4 realizations for each clump, and find $\mu_{1/2}(\delta_{nns})=0.118$ pc with $\mu_{1/2}(\delta_{nns})/\mu_{1/2}(\delta'_{nns})=1.42$ and a (16, 84) percentile interval of

(0.065, 0.232) pc. For comparison, if we assume that all sources are uniformly distributed within a spherical volume of radius R_s , the following projection correction may be applied:

$$\delta_{\rm nns} = \delta_{\rm nns}' \left(\frac{4R_{\rm s}}{3\delta_{\rm nns}'} \right)^{1/3},\tag{3}$$

as is done in Myers (2017). If we assume $R_s = 0.38$ pc from the radius of the 20% power point of the ALMA primary beam at 4 kpc, then this correction factor would be $\delta_{nns}/\delta'_{nns} \approx 1.84$ and $\delta_{nns} = 0.153$ pc, which is larger than the median value computed above from the MC trials by 29%.

5.2. Jeans Length Comparison

To consistently compare δ_{nns} values between clumps with different physical conditions, we scale the values by the clump average thermal Jeans length, the minimum wavelength for gravitational fragmentation in an isothermal, uniform medium. The thermal Jeans length $\lambda_{j,th}$ can be expressed as (McKee & Ostriker 2007):

$$\lambda_{\rm j,th} = \left(\frac{\pi c_{\rm s}^2}{G\rho_0}\right)^{1/2},\tag{4}$$

where $c_{\rm s}=\sqrt{kT/\mu m_{\rm p}}$ is the isothermal sound speed (0.21 km s⁻¹ for $T_{\rm d}=12$ K), G is the gravitational constant, and ρ_0 is the average volume density. For the accurate propagation of uncertainties in the calculation of $\lambda_{\rm j,th}$, we perform MC random sampling of the relevant observational uncertainties in ρ_0 from the dust mass surface density ($\rho_0=3\Sigma/4R$) and heliocentric distance. The total (i.e., gas) mass surface density is calculated with

$$\Sigma = \frac{S_{\nu, \text{int}}}{B_{\nu}(T_{\text{d}})f_{\text{d}} \kappa \mu m_{\text{p}} \Omega},\tag{5}$$

for source integrated flux density $S_{\nu, \rm int}$, source solid angle Ω , Planck function $B_{\nu}(T_{\rm d})$ evaluated at dust temperature $T_{\rm d}$, opacity per mass of dust $\kappa(\lambda=1.3~{\rm mm})=0.90~{\rm cm^2~g^{-1}}$ (Ossenkopf & Henning 1994), mean molecular weight $\mu=2.33$, and dust-to-gas mass ratio $f_{\rm d}\equiv (m_{\rm d}/m_{\rm g})=1/110$ (values are further described in Appendix C).

The fragmentation measured within the ALMA maps is most sensitive within the HPBW (27") of the primary beam, so we consider an estimate of ρ_0 within this volume to be the most representative density for the computation of $\lambda_{i,th}$. Clump average densities on angular scales ($\sim 1'-2'$) larger than the HPBW likely underestimate ρ_0 . Likewise, image-integrated flux densities from the 12 + 7 m array data may underestimate the Σ from spatial filtering. Due to the unfavorable match in resolution compared to the Hi-GAL 500 μ m ($\theta_{hpbw} \approx 35''$) or BGPS 1.1 mm ($\theta_{hpbw} \approx 33''$), we extract flux densities from the ATLASGAL 870 μ m maps ($\theta_{hpbw} \approx 19''$) at the position of the ALMA pointing for each clump within a beam-sized 27" diameter circular aperture to measure Σ_{cl} . Use of the singlemillimeter flux mitigates one systematic uncertainty in choosing between Hi-GAL SED fits with or without the 160 μ m band included, or using Hi-GAL SED fits that are over the emission for the full clump rather than the peak at consistent angular resolution. The clump average dust temperatures from SED fits to the Hi-GAL data range from

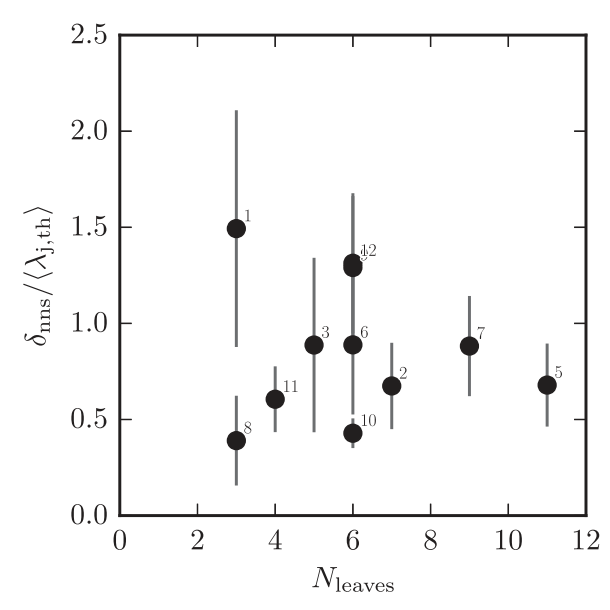


Figure 11. Nearest neighbor separation scaled by the clump thermal Jeans length $(\delta_{nns}/\langle \lambda_{j,th} \rangle)$ vs. number of leaves.

 $T_{\rm d} = 10$ –14 K, but some systematic uncertainty exists with averaging over larger volumes than the ALMA field of view and choices in including the 160 μ m band. We choose a conservative dust temperature distribution by assuming a Gaussian dust temperature distribution $\langle T_{\rm d} \rangle = 12 \pm 2 \, {\rm K} \, (1\sigma)$ interval). For consistency, this temperature is also used for the gas kinetic temperature in c_s . We propagate the uncertainty in heliocentric distance based on the distance probability density function (DPDF) from Ellsworth-Bowers et al. (2015) for each clump. All sources are well-resolved to the near kinematic distance, and have a $\delta d_{\odot}/d_{\odot} \approx 0.15$ fractional uncertainty. We sample the distributions for S_{870} , $T_{\rm d}$, and d_{\odot} for each MC trial of ρ_0 in the calculation of $\lambda_{\rm j,th}$, to combine with a trial of $\delta_{\rm nns}$ in order to compute the quotient $\delta_{\rm nns}/\langle \lambda_{\rm i,th} \rangle$ for each clump. The computed median volume densities for the clumps in the sample range between $n(H_2) = (2-6) \times 10^4 \text{ cm}^{-3}$, with associated values of the thermal Jeans length between $\lambda_{i,th}$ = 0.10–0.17 pc (2.1– 3.5×10^4 au). The median of samples from all clumps is $\lambda_{i,th} = 0.135$ pc (2.77 \times 10⁴ au). No correlation is observed between $\delta_{\rm nns}/\langle \lambda_{\rm i,th} \rangle$ and the number of cores/ leaves in each clump (Figure 11).

Probability density functions (PDFs) of $\delta_{nns}/\langle \lambda_{j,th}\rangle$ are computed for each clump by performing Monte Carlo random sampling of the observational uncertainties in $\lambda_{j,th}$ as described above and sampling the deprojected source separations (see Section 5.1). Figure 12 (left) shows the distributions of $\delta_{nns}/\langle \lambda_{j,th}\rangle$ for each clump, sorted in descending order by the number of continuum sources. The separation distributions show a bimodal tendency with peaks at $\delta_{nns}/\langle \lambda_{j,th}\rangle \sim 0.3$ and $\delta_{nns}/\langle \lambda_{j,th}\rangle \sim 1$, and with long tails extending to high values $\gtrsim 1.5$. The distinct peaks at small values of $\delta_{nns}/\langle \lambda_{j,th}\rangle$ (all well-resolved) likely result from closely spaced, connected sources where δ_{nns} is not strongly affected from sampling the inclination distribution. Median values of the distributions range between $\delta_{nns}/\langle \lambda_{j,th}\rangle = 0.4-1.5$. The values are generally consistent with the thermal Jeans length, but the high frequency of sources with

sub-Jeans separations may indicate hierarchical fragmentation at multiple scales. With the initial fragmentation on the clump scale, a further fragmentation on the "core scale" would proceed on sizes $\lesssim\!\!2\times10^4$ au and densities $\gtrsim\!\!3\times10^5\,\mathrm{cm}^{-3}$. If such hierarchical fragmentation proceeds principally with two resultant fragments on the core scale, then the second-nearest neighbor distance would measure the above level in the hierarchy and recover the spacing of the clump scale. This is supported by a plot of the second-nearest neighbor distance $\delta_{\mathrm{nns}}^{(2)}$ distributions, shown in Figure 12 (right), that shows clumps with more unimodal distributions, with modes and median values at or slightly above the thermal Jeans length. Median values of the $\delta_{\mathrm{nns}}^{(2)}$ distributions are greater than those for δ_{nns} but generally fall within a similar range between $\delta_{\mathrm{nns}}^{(2)}/\langle \lambda_{\mathrm{j,th}}\rangle = 0.75-1.7$.

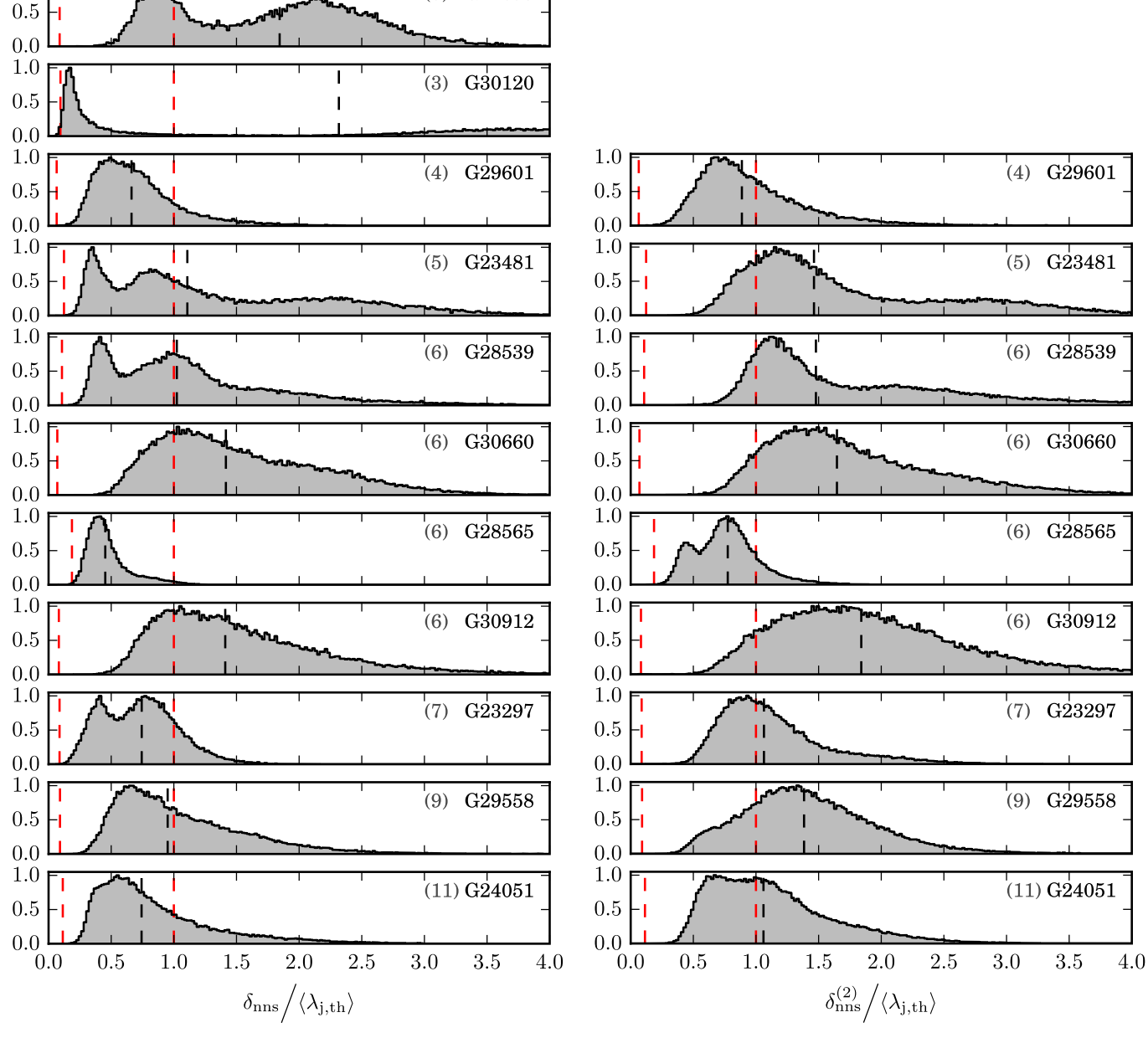
We compute PDFs for each clump (see above) and the ensemble distribution composed of all separation measurements from each clump aggregated together (Figure 13). The ensemble separation distribution is used to define a representative fragmentation scale from the SCCs in this survey. As these clumps are at similar distances and blindly selected from Galactic plane dust continuum surveys, the measured ensemble sample properties may be used to cautiously infer the properties of the Galactic high-mass SCC population $(M_{\rm cl} \gtrsim 10^3 \, M_{\odot})$. Additional observations are required to directly constrain the properties of SCCs with $M_{\rm cl} \gtrsim 10^4 \, M_{\odot}$ (if they exist outside of the Central Molecular Zone) or SCCs below the mass range of this sample, $M_{\rm cl} \lesssim 400\,M_{\odot}$. Figure 13 shows the cumulative distribution function (CDF) for the ensemble of $\delta_{\rm nns}/\langle \lambda_{\rm i,th} \rangle$ measurements as drawn from the MC sampling for the projected separations, projection-corrected separations, and relevant scales such as the resolution and primary beam HPBW. The projection-corrected ensemble distribution has a median value of $\delta_{\rm nns}/\langle \lambda_{\rm j,th} \rangle = 0.82$, with a (25, 75) percentile interval of 0.52–1.25. The percentiles for $\delta_{nns}/\langle\lambda_{j,th}\rangle=$ 0.5, 1, 2, and 3 are 23.6, 63.3, 90.3, and 97.4, respectively. Overall, the sample of SCCs show a fragmentation scale that is wellcharacterized by the thermal Jeans length.

A relatively small fraction of the separation distribution is inconsistent with the thermal Jeans length: <10% for >2 × $\lambda_{\rm j,th}$. The large separations do not result from a single or a small number of clumps with consistently large separations, but rather from isolated individual sources within clumps that show fragmentation near the thermal Jeans length. G30660 and G30912, for example, have a significant proportion of the distribution at large separations (see Figure 12, left), but do not have peculiar dust temperatures (between $T_{\rm d}=11$ –12 K from Hi-GAL SED fits). This portion of the separation distribution may indicate an additional scale for hierarchical fragmentation where a source of nonthermal support prevents fragmentation at the thermal Jeans scale.

The Jeans length can further take into account sources of nonthermal support, such as turbulence or magnetic fields, by using an effective sound speed

$$c_{\text{s,eff}} = (c_{\text{s}}^2 + \sigma_{\text{nt}}^2)^{1/2}$$
 (6)

through the contribution of a nonthermal velocity dispersion $\sigma_{\rm nt}$. From S16, 9 out of 12 clumps have $T_{\rm K}$ measured from NH₃ (at 32" resolution). The measured velocity dispersions (i.e., $c_{\rm s,eff}$) determined from the spectral line model fit range between $\sigma({\rm NH_3}) = 0.50 - 0.95~{\rm km~s^{-1}}$, with a median value of



(3) G22695

Figure 12. Left: PDFs of the projection-corrected nearest neighbor separations between sources in each clump, scaled by the clump average thermal Jeans length. PDFs are scaled such that the peak probability equals unity. Thermal Jeans length is shown with a dashed red line at 1 (~0.1 pc). Dashed red line near zero shows the scale of the synthesized beam (~0.015 pc), and the black dashed line shows the 50th percentile of the distribution. Source names are shown in the upper right, and the number of sources in parentheses. Right: PDFs for the second-nearest neighbor separations ($\delta_{nns}^{(2)}$). The distributions are more unimodal near unity and show moderately larger median separations than δ_{nns} .

 $0.65~{\rm km~s^{-1}}$, corresponding to $\sigma_{\rm nt}\approx 0.62~{\rm km~s^{-1}}$ for $c_{\rm s}=0.21~{\rm km~s^{-1}}$ at $T_{\rm K}=12~{\rm K}$ (where $T_{\rm K}=11$ –14 K). Replacing $c_{\rm s}$ with $c_{\rm s,eff}$ in Equation (4) yields the effective Jeans length, or when turbulence is the dominant source of nonthermal support, the turbulent Jeans length $\lambda_{\rm j,tu}$. Because $\lambda_{\rm j} \propto c_{\rm s}$, the increase of $c_{\rm s,eff}/c_{\rm s} \sim 2.4$ –4.5 (median 3.1) yields a similar scaling for $\lambda_{\rm j,tu}/\lambda_{\rm j,th}$. In comparison, $\delta_{\rm nns}/\langle\lambda_{\rm j,th}\rangle=3~(\delta_{\rm nns}/\langle\lambda_{\rm j,tu}\rangle\approx0.32)$ occurs at the 97.4 percentile, and thus while such separations are not absent from the data, they are also not representative of the fragmentation measured within the ALMA maps. The length scale distribution is incomplete beyond $\delta_{\rm nns}/\langle\lambda_{\rm j,th}\rangle>3.1$, where 10%

of the MC trials would have 3D separations greater than or equal to the FOV (40'').

6. Discussion

The physical processes regulating fragmentation in molecular clouds remain an open problem in star formation. How much are SCCs supported against gravitationally induced fragmentation from nonthermal forms of pressure, such as magnetic fields (*B*-fields) and/or turbulence? Individual SCCs have been studied at high resolution (Beuther et al. 2015a; Sanhueza et al. 2017), but we shall discuss a systematic set of

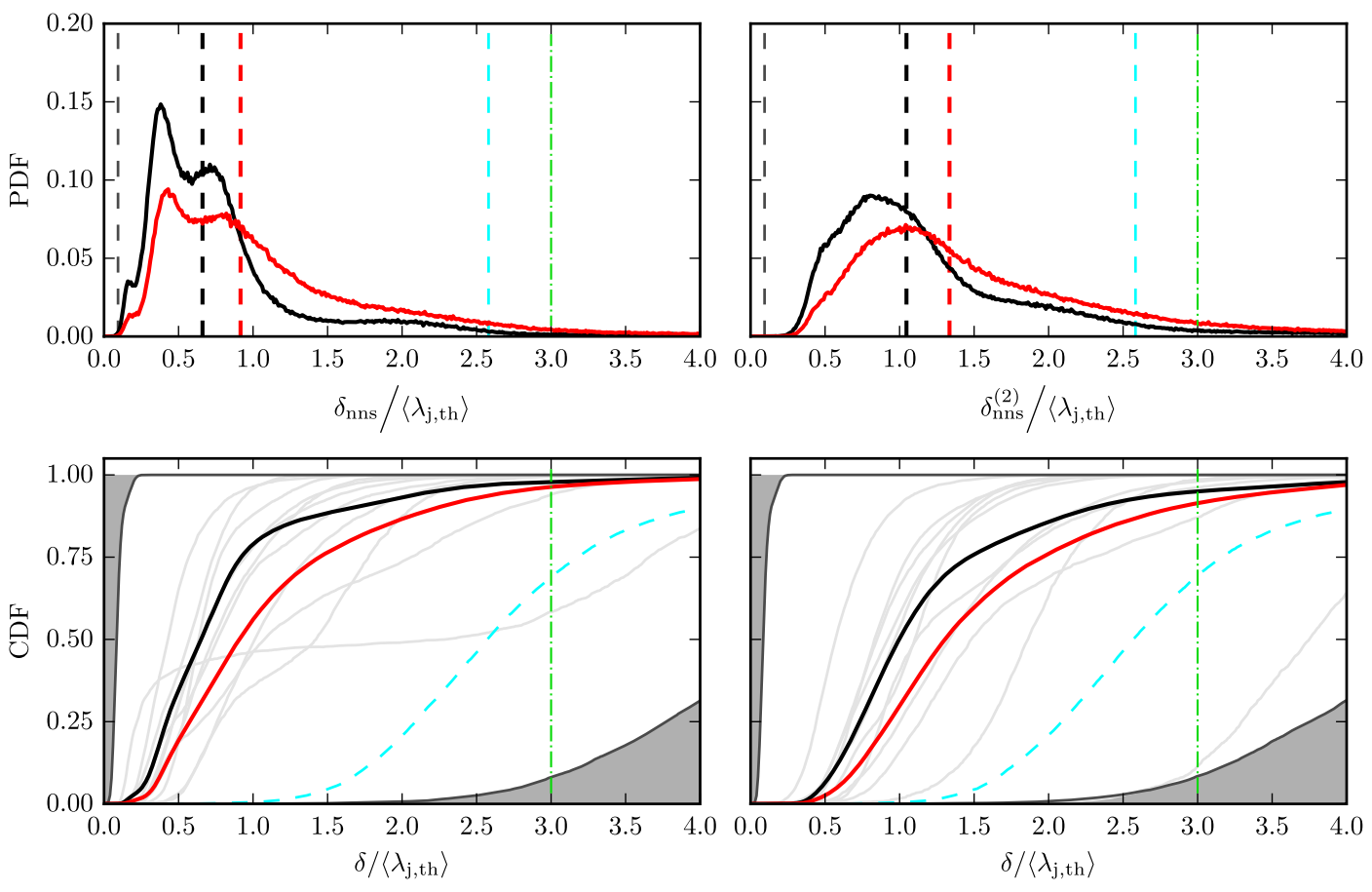


Figure 13. Lower left: CDFs of different lengths δ when scaled as multiples of the thermal Jeans length computed with Monte Carlo random sampling. These are CDFs of the projection-corrected nearest neighbor separations for sources in all clumps (red), for sources of individual clumps (thin gray), and projected nearest neighbor separations for all sources (black). The median value of $\delta_{nns}/\langle \lambda_{j,th}\rangle=0.82$, with a (25,75) percentile interval from 0.52–1.25, consistent with fragmentation primarily occurring at the thermal Jeans length on the clump scale. The value $\delta_{nns}/\langle \lambda_{j,th}\rangle=2$ occurs at the 90.3 percentile. The dashed–dotted green line visualizes the median value turbulent Jeans length of $\lambda_{j,tt}/\lambda_{j,th}\approx3$. The inner and outer gray areas show the scaled synthesized beam (0.18) and scaled 20% point of the primary beam (40"). The scaled HPBW (27") of the primary is also shown (dashed cyan). Upper left: PDFs of different length scales δ , with the same color coding. Dashed lines show the values of the 50th percentiles. Lower right: CDF for the second-nearest neighbor separations, $\delta_{nns}^{(2)}$. Upper right: PDF for the second-nearest neighbor separations, $\delta_{nns}^{(2)}$.

observations on a representative sample of high-mass SCCs. Here, we describe the fragmentation characteristics of SCCs in the context of theoretical models of star and cluster formation, and compare them to existing high-resolution observations of clumps and IRDCs.

6.1. Cylindrical Fragmentation in SCCs

As shown in Section 5, we find that clumps fragment at scales consistent with the thermal Jeans length in SCCs. It is known, however, that geometry and nonthermal support affect the predicted fragmentation scale, producing deviations from that expected for an isothermal, uniform medium. In this section, we discuss how the fragmentation scale observed with ALMA compares to different characteristic length scales.

Filaments are ubiquitous in both observed molecular clouds and simulations (e.g., Barnard 1907; André et al. 2014; Smith et al. 2016), and thus cylindrical geometry is of special significance to dense molecular regions. On larger spatial scales observable in MIR extinction, it is clear that the clump peaks are embedded in filamentary gas structures (see Figure 1 and G23297, for a good example). An infinite, self-gravitating cylinder is unstable to axisymmetric perturbations or "sausage" instability, where the cylinder fragments at the scale of the fastest-growing

mode of the fluid instability (Chandrasekhar & Fermi 1953; Ostriker 1964; Larson 1985; Nagasawa 1987; Inutsuka & Miyama 1992). For a pressure-confined isothermal gas cylinder of radius R and scale height $H=c_{\rm s}(4\pi G\rho_{\rm c})^{-1/2}$ (where $\rho_{\rm c}$ is the central density of the cylinder), the fastest-growing mode depends on the ratio of R and H (Nagasawa 1987). In the case where $R\ll H$, then $\lambda_{\rm cyl}\approx 10.8R$; alternatively, where $R\gg H$, then $\lambda_{\rm cyl}\approx 22.4H$ (Nagasawa 1987; Jackson et al. 2010).

Is the isothermal, cylindrical fragmentation scale representative in SCCs? The approximation of SCCs as isothermal is imperfect due to shielding that decreases the temperatures of inner regions, but the assumption is generally more valid than clumps with active HMSF and substantial internal protostellar heating and feedback. Observed aspect ratios of \gtrsim 5 over the full clump extent support the approximation of an infinite cylindrical geometry. The typical radial extent of the SCCs as observed in the MIR extinction maps suggests $R \sim 0.4$ pc. Assuming that the cylinder central density is equal to the observed clump peak density (i.e., $\rho_{\rm c} = \rho_0 \approx 3 \times 10^4 \, {\rm cm}^{-3}$), then $H \sim 0.02$ pc, and thus $R/H \sim 20$ roughly satisfies the condition $R \gg H$. Note that, for $\rho_{\rm c}$ equal to the clump peak density, this simplifies to $\lambda_{\rm cyl}/\lambda_{\rm j,th} \approx 3.50$, or for the median $\lambda_{\rm j,th} = 0.137$ pc, $\lambda_{\rm cyl} = 0.480$ pc. We find that $\lambda_{\rm cyl}$ is not

representative of the δ_{nns} distribution in SCCs, with the observed $\delta_{nns}/\langle \lambda_{j,th} \rangle \sim 1$.

Observational studies carried out on larger spatial scales than this work support λ_{cyl} as a characteristic scale in filaments (Beuther et al. 2015b; Friesen et al. 2016). While these studies did not have sufficient spatial resolution to adequately resolve the thermal Jeans length, they probe separations on the clump scale and larger than ~ 1 pc, as observed with ALMA. This work complements the larger-scale studies by identifying fragmentation on the clump Jeans length at an early evolutionary phase. This is supported by the results of Kainulainen et al. (2013), who use Spitzer MIR extinction mapping to find that the molecular filament G11.11-0.12 is described well by filament fragmentation and turbulent λ_{cvl} on $\delta \gtrsim 0.5$ pc and $\lambda_{i,th}$ on smaller scales. Beuther et al. (2015b), in an analysis of the fragmentation in the star-forming filament IRDC 18223, find a mean fragment separation of $\delta = 0.40 \pm$ 0.18 pc, consistent with a thermal $\lambda_{cyl} = 0.44$ pc of the filament, approximately twice that of $\lambda_{i,th} = 0.07-0.23$ pc. However, the authors note that measures of δ should be considered an upper limit, due to the sensitivity and resolution of the data. Friesen et al. (2016), in a survey of the entire Serpens South molecular cloud (as part of the GBT Ammonia Survey, GAS; Friesen et al. 2017), find that the nearest neighbor separations of dense gas structures within the same filament are significantly larger than $\lambda_{i,th}$ and are wellrepresented by $\lambda_{\rm cyl}$. The spatial resolution is limited to approximately $\lambda_{\rm j,th} \sim 0.07~{\rm pc}$, however, and thus does not properly resolve $\lambda_{i,th}$ in sources with $\langle n \rangle \gtrsim 2 \times 10^3 \, \text{cm}^{-3}$. The above surveys support the view of hierarchical fragmentation by gravitationally unstable filaments, but lack the resolution to test what fragmentation process dominates on the scales of individual cores embedded within the clumps. The measurements of the fragmentation scale presented in Section 5 complement the above studies at resolutions down to ~3000 au and provide further support for the view that filaments initially fragment at $\lambda_{\rm cyl}$ and then fragment further at $\lambda_{\rm i,th}$.

6.2. Comparison to More Active Regions

Direct observations of star-forming IRDCs and embedded protoclusters have found fragmentation consistent with the thermal Jeans length (Beuther et al. 2015a, 2018; Palau et al. 2015; Busquet et al. 2016; Teixeira et al. 2016), but it is unknown if these systems represent the initial state of fragmentation. Because high-mass SCCs may represent an initial stage of protocluster evolution before the formation of a high-mass star, they offer unique insight into the physical processes regulating fragmentation when compared to more evolved systems. From a survey of dense, star-forming cores, Palau et al. (2015) find that the fragmentation on \sim 0.1 pc scales is explained best through thermal fragmentation. These results are similar to those found at subcore spatial scales of ≤1000 au toward the Orion Molecular Cloud 1S (OMC-1S; Palau et al. 2018), and also consistent with the fragmentation measured in OMC-1N (Teixeira et al. 2016). While the measured median nearest neighbor separation in SCCs is consistent with the thermal Jeans length of the clump gas, the distribution also shows a distinct peak at approximately an order of magnitude higher gas density near $\delta_{nns}/\langle\lambda_{j,th}\rangle\approx 0.3$ (see Figures 12 and 13). These results may indicate continued thermal Jeans fragmentation, such as observed in OMC-1S and OMC-1N. Beuther et al. (2015a) find results that are approximately

consistent with thermal Jeans fragmentation toward the $\sim 800 \, M_{\odot}$ IRDC 18310–4, and while showing faint 70 μ m emission, exhibit physical properties similar to those of the SCCs in this sample. Similarly, an analysis of the star-forming IRDC G14.225-0.506 favors thermal Jeans fragmentation (Busquet et al. 2016). Beuther et al. (2018) present a minimal spanning tree analysis of the separations in the CORE survey of 20 luminous ($L_{\rm bol} > 10^4 L_{\odot}$) high-mass star-forming regions, and find fragmentation at scales on the order of the thermal Jeans length or smaller. As a possible explanation for the sub-Jeans length scales, Beuther et al. (2018) suggest that bulk motions from ongoing global collapse may have brought the fragments within closer proximity after having initially fragmented on the thermal Jeans scale. All of the sources in the CORE survey are high-mass protostellar objects (HMPOs) and more evolved than this sample. Thus, our finding of fragmentation on the thermal Jeans length at an earlier evolutionary stage supports both the interpretation of the COREs results and the conclusion that the measured fragmentation scale may be impacted by the dynamical evolution of the protocluster.

The agreement between the nearest neighbor separations and the thermal Jeans length appears to favor a Jeans fragmentation process for stellar cluster formation. Indeed, the thermal Jeans mass in typical star-forming clumps is approximately $1 M_{\odot}$, which corresponds well with the stellar mass at the peak of the IMF. Therefore, Larson (2005) argued that the thermal Jeans process is responsible for the formation of lower-mass stars in a cluster. Zhang et al. (2009) found that cores forming massive stars often have $\gtrsim 10 M_{\odot}$, an order of magnitude greater than the thermal Jeans mass of its parental clump. These cores require additional support from turbulence to account for their formation. Furthermore, the observed measurements imply that thermal physics provide the dominant form of support, but additional models exist to describe the thermal fragmentation process that differ in geometry and density profile. For example, Myers (2017) present 2D axisymmetric models of filamentary structure that fragment through the thermal instability of Bonnor-Ebert spheres above a threshold minimum density. Because the Bonnor-Ebert radius and Jeans length have the same dependence on temperature and density, with only slight differences in numerical coefficients, this leads to a fragmentation approximately equal to $\lambda_{j,th}$. When compared to the observed median $\delta_{\rm nns}/\langle \lambda_{\rm i,th} \rangle = 0.91$ from Section 5, the spacings between cores predicted by Myers (2017), $\delta_{\rm nns}/\langle \lambda_{\rm j,th} \rangle = 0.71$ (for a concentration factor $q_{\rm Z} \equiv$ $\langle n \rangle / n_{\rm min} = 2$), are broadly consistent.

6.3. Coeval Formation of Low- and High-mass Protostars?

It is not clear if SCCs are the progenitor environments of high-mass star formation. Their high total masses ($M_{\rm cl} \sim 1000 \, M_{\odot}$), high central densities ($\langle n \rangle \sim 5 \times 10^4 \, {\rm cm^{-3}}$), cold gas kinetic temperatures ($\langle T_{\rm K}({\rm NH_3}) \rangle \sim 11 \, {\rm K}$), and low virial parameters ($\alpha_{\rm vir} \sim 0.1$ –1) (Wienen et al. 2012; Svoboda et al. 2016) all point to persistent, bound clumps with the likely necessary physical conditions for high-mass star formation (McKee & Ostriker 2007). However, no high-mass protostars are observed. These observational facts are consistent with a scenario where high-mass stars form in SCCs through thermal fragmentation, and then accrete clump gas as initially low-mass protostars. Thus, SCCs may represent a very early and unique stage in protocluster evolution preceding the formation of high-mass protostars. This view is supported by cluster-scale theoretical simulations that

incorporate protostellar and stellar feedback (Smith et al. 2009; Peters et al. 2010a, 2010b, 2011; Wang et al. 2010). Smith et al. (2009) find that no high-mass starless cores are formed in their models, and that massive stars originate from low- to intermediate-mass cores that become high-mass protostars via accretion. The mass accreted comes primarily from the surrounding clump at scales >0.1 pc (Smith et al. 2009; Wang et al. 2010).

Cyganowski et al. (2017), in a study toward the deeply embedded protocluster G11.92-0.61, discover low-mass cores in the accretion reservoir of the accreting HMPO "MM1" with mass $M_* \sim 30\text{--}60 \, M_\odot$ (Ilee et al. 2016). The detection of coeval low- and high-mass protostars is consistent with competitive accretion-type models of star formation (see Section 1). At a comparable distance of $d_{\odot} = 3.37^{+0.39}_{-0.32}$ kpc (derived from maser parallax by Sato et al. (2014)) and total mass to the SCCs in this study, G11.92–0.61 is more evolved, coincident with several indicators of high-mass star formation, such as Class I and II CH3OH masers, H2O masers, a GLIMPSE Extended Green Object (Cyganowski et al. 2008), numerous "hot core" molecular lines, and high-velocity collimated outflows. The sample of SCCs in this study complements the study of G11.92-0.61 in Cyganowski et al. (2017) through ALMA observations at similar resolution and sensitivity for clumps in a less active evolutionary state. In contrast, we find no clear high-mass protostellar cores or highmass protostars in our sample of SCCs, while numerous accreting low-mass protostars are observed, as evidenced by bipolar outflows in CO/SiO. If a few of the protostars in SCCs will accrete up to high-mass stars, for which the accretion reservoir of the clump is sufficient, then these observations support a coeval mode of protocluster formation at earlier phases. When initially only low- to intermediate-mass protostars are present, this coeval formation may also be termed "low-mass first," in contrast to the monolithic collapse of turbulently supported high-mass cores. The competitive accretion-type simulations performed by Smith et al. (2009) find that high-mass stars form initially from intermediate-mass prestellar cores near the center of the gravitational potential, which accrete principally from collapsing clump gas up to high-mass condensations. An important feature of the Smith et al. (2009) model is that low-mass protostars form within the accretion reservoir of the central protostar, at separations < 0.15 pc. This is matched well to the distribution of nearest neighbor separations found in this work: $\mu_{1/2}(\delta_{\rm nns}) = 0.118~{\rm pc}$ (see Section 5). As Smith et al. (2009) point out, this signature is likely the most detectable at the early evolutionary phases of the clump, where sources are less centrally concentrated in the potential and bright sources of emission are not present.

In contrast to the results of Cyganowski et al. (2017), Zhang et al. (2015) studied the protocluster G28.24+0.06 P1 and failed to detect a distributed population of low-mass cores with Cycle 0 ALMA observations. Based on this, Zhang et al. (2015) draw the conclusion that the distributed population of low-mass cores forms at a later evolutionary stage and that they are not, at least for the initial generation of protostars, coeval. Because G11.91–0.61 is at a later evolutionary stage, the distributed population of low-mass protostars observed in it may have developed after the massive cores formed. The SCCs in this study are in an early evolutionary phase similar to that of G28.24+0.06, and they also similarly lack high-mass protostars (the maximum core mass in G28.4+0.06 is

 $M_{\rm core} \sim 16\,M_{\odot}$). Accurate core masses are required for a quantitative analysis of the mass segregation and related length scales, but the diversity in morphologies shown within the sample, from distributed (e.g., G30660, G29558) to weakly fragmented (e.g., G28539, G29601), supports the presence of a distributed low-mass core population at the initial evolutionary phase for some systems. It is possible that, depending on the initial level of support provided against fragmentation, individual systems develop with varying degrees of hierarchy and segregation, and that the conclusions of Zhang et al. (2015) and Cyganowski et al. (2017) may both be correct for sources of different initial physical conditions.

The short evolutionary timescales of high-mass starless clumps, $\tau_{\rm SCC} \sim 0.5$ –0.1 Myr for $M_{\rm cl} = 1$ –3 \times 10³ M_{\odot} S16, is also consistent with the simulations of Smith et al. (2009), which show that the central, resultant high-mass protostar accretes in 0.25 \times $t_{\rm dyn} \sim 0.12$ Myr the clump dynamical time, over a diameter of ~0.4 pc (equivalent to the ALMA HPBW) (see also Wang et al. 2010). Similarly, Battersby et al. (2017) perform a lifetime analysis of dense, molecular gas $(N({\rm H_2}) \gtrsim 10^{22}~{\rm cm^{-2}})$ analyzed on a per-pixel basis from a Hi-GAL $2 \deg \times 2 \deg$ field near $\ell = 30 \deg$. They find a timescale that is consistent for starless regions of 0.2–1.7 Myr, although with substantial uncertainty. The similarity in timescales is reasonable, as once a high-mass protostar forms, it would be accompanied by observational star formation indicators that identify it as a protostellar clump and remove it from the SCC category, as determined in \$16. Further, we also observe hierarchical fragmentation as evidenced by the multimodal distribution of nearest neighbor separations (see Figure 13), as seen in G11.92-0.61. The ubiquity of filamentary structures observed (see Figure 3) may also point to accretion mediated by subsonically gravitationally contracting filaments (Smith et al. 2016). This may suggest that, while self-gravitating, turbulent clumps are not globally collapsing, and therefore accretion may yet be mediated through locally collapsing filaments. This latter point will be the topic of further research investigated with ALMA observations of N₂H⁺ $J=1 \rightarrow 0$ to study the kinematics of the filaments observed in this sample SCCs.

7. Conclusions

We present the first systematic observations of a large sample of well-vetted starless clump candidates with ALMA at high resolution (~ 3000 au) capable of resolving the thermal Jeans length and sensitivity ($50~\mu\rm Jy~beam^{-1}$) necessary for detecting point sources down to $\sim 0.3~M_{\odot}$ and moderately compact starless cores down to $\sim 1.0~M_{\odot}$). The targets are selected from a complete sample of clumps identified from large Galactic plane surveys. The sample is composed of 12 high-mass SCCs within 5 kpc, from Svoboda et al. (2016) and Traficante et al. (2015), that did not show detected emission at 70 $\mu\rm m$ or other indicators of star formation. Because these systems have not been affected by the extreme (proto-)stellar feedback of high-mass stars, they are ideal environments to study the initial conditions of protocluster evolution. Our main findings are:

1. The newly sensitive ALMA Band 6 12 + 7 m ($\nu_c \approx 230 \ \text{GHz}$) data show multiple indicators of low-/intermediate-mass star formation activity present in 11 out of 12 formerly starless clump candidates. This is determined through the presence of bipolar outflows

detected in CO $J=2 \rightarrow 1$ and SiO $J=5 \rightarrow 4$ emission, as well as high-excitation p-H₂CO $3_{2,2} \rightarrow 2_{2,1}$ emission ($E_{\rm u}/k=68.1$ K). These observations caution the interpretation of infrared dark clouds and SCCs identified from Galactic plane surveys as quiescent, and unless shown otherwise are, given the findings toward this sample, likely to host low-/intermediate-mass star formation activity below the luminosity completeness of current surveys.

- 2. We compare representative examples of resolved and unresolved continuum sources with radiative transfer models of starless cores computed with RADMC-3D. Unresolved sources are poorly fit by starless core models with typical physical properties. The range of models does not encompass the most compact and dense cores $(R_{\rm flat} < 1 \times 10^3 \, {\rm au}, \, n_{\rm in} \gtrsim 1 \times 10^7 \, {\rm cm}^{-3})$, but the short core freefall times $(t_{\rm ff} \lesssim 1 \times 10^4 \, {\rm yr})$ and the observation of a flux density similar to that of Gould's Belt low-/intermediate-mass protostars, support the conclusion that these cores are protostellar even without identified outflows in CO or SiO.
- 3. Two high-mass starless core candidates in G28539 are identified and well-fit by starless core models, with $M_{\rm S2} = 29_{15}^{52} \, M_{\odot}$ and $M_{\rm S4} = 14_{6.0}^{34}$. Without supplementary measurements to infer the dust temperature profile, the masses are highly uncertain, and are consistent within the uncertainties of only forming an intermediate-mass star ($M_{*} < 8 \, M_{\odot}$).
- 4. G28539 is the sole remaining starless clump candidate without any definitive indications of protostellar activity from the ALMA observations. It is the most massive SCC in the sample ($M_{\rm cl} \approx 3600^{+600}_{-500}\,M_{\odot},\,d_{\odot} = 4.8^{+0.3} 0.3\,{\rm kpc}$), and stands as an excellent target to study the initial conditions of protocluster evolution. A marginal 24 μ m source, however, is observed coincident with 1.3 mm continuum source (G28539 S1) near the NW edge of the ALMA field, which may be evidence of protostellar activity. Further indirect evidence for star formation exists from compact SiO and CH₃OH emission, although the source of emission is not associated with a continuum source. If these signatures are indeed associated with protostellar activity, there would be no true high-mass starless clumps in this sample.
- 5. A high degree of fragmentation is observed, with nearest neighbor separations consistent with the clump scale thermal Jeans length (~0.1 pc). In the context of previous observations that, on larger scales, see separations consistent with the turbulent Jeans length or cylindrical thermal Jeans length, our findings support a hierarchical fragmentation process, where the highest-density regions of SCCs are not strongly supported against fragmentation by turbulence or magnetic fields.
- 6. Observed embedded low- to intermediate-mass star formation and thermal Jeans fragmentation in high-mass SCCs are consistent with models of star formation that form high-mass stars through gravitationally driven cloud inflow, in which low- and high-mass stars form coevally. However, further observations and follow-up study are necessary to properly characterize the clump star formation efficiency, protostellar accretion rates, and presence of dynamical flows in molecular tracers, to validate this conclusion.

We are grateful to the anonymous referee for many helpful comments and suggestions. B.E.S. would like to thank Al Wootten and the staff of the NRAO North American ALMA Science Center, Kimberly Ward-Duong for helpful discussions, and Viviana Rosero for access to the JVLA C Band image toward G28539. B.E.S. was supported in part by the NSF Graduate Research Fellowship under grant No. DGE-114395. Y.L.S. and B.E.S. acknowledge support from NSF AAG grant No. AST-1410190. H.B. acknowledges support from the European Research Council under the European Community's Horizon 2020 framework program (2014-2020) via the ERC Consolidator Grant "From Cloud to Star Formation (CSF)" (project number 648505). This paper makes use of the following ALMA data: ADS/JAO.ALMA#2015.1.00959.S. ALMA is a partnership of ESO (representing its member states), NSF (USA) and NINS (Japan), together with NRC (Canada), MOST and ASIAA (Taiwan), and KASI (Republic of Korea), in cooperation with the Republic of Chile. The Joint ALMA Observatory is operated by ESO, AUI/NRAO and NAOJ. The National Radio Astronomy Observatory is a facility of the National Science Foundation operated under cooperative agreement by Associated Universities, Inc.

Facility: ALMA.

Software: This research has made use of the following software projects: Astropy¹⁸ (The Astropy Collaboration et al. 2018), Matplotlib¹⁹ (Hunter 2007), NumPy²⁰ and SciPy²¹ (Oliphant 2007), Pandas²² (McKinney 2010), IPython²³ (Pérez and Granger 2007), CASA²⁴ (McMullin et al. 2007), and NASA's Astrophysics Data System.

Appendix A Example CO Outflow Analysis

The CO $J=2 \rightarrow 1$ image cubes show complex emission structures that complicate the identification of coherent velocity structures, such as outflows. Effects may be observed from spatial filtering, foreground and background clouds, and strong selfabsorption at the clump systemic velocities. Bipolar outflows with red- and blueshifted velocity components may still be easily observed in the data, however, because they are bright and are coherent in velocity over many independent channels. To illustrate these effects, we present a spatially averaged spectrum and position-velocity diagram (PV; Figure 14) for the prominent NW-SE outflow originating from G24051 S4 (see Figure 7). The spectrum and PV diagram are extracted from a 6."0 diameter rectangular aperture centered along the outflow axis. Figure 14 shows bright, extended emission spanning up to $\sim 20 \text{ km s}^{-1}$ from the center LSR velocity of $v_{lsr} = 83 \text{ km s}^{-1}$ determined from the dense gas tracer $H_2CO\ 3_{0,3} \to 2_{0,2}.$ The redshifted lobe (SE) and blueshifted lobe (NW) are clearly observed in the PV diagram at negative and positive angular offsets along the rectangular aperture axis.

¹⁸ https://astropy.org/

¹⁹ https://matplotlib.org/

²⁰ http://www.numpy.org/

²¹ https://scipy.org/

²² https://pandas.pydata.org/

²³ https://ipython.org/

https://casa.nrao.edu/

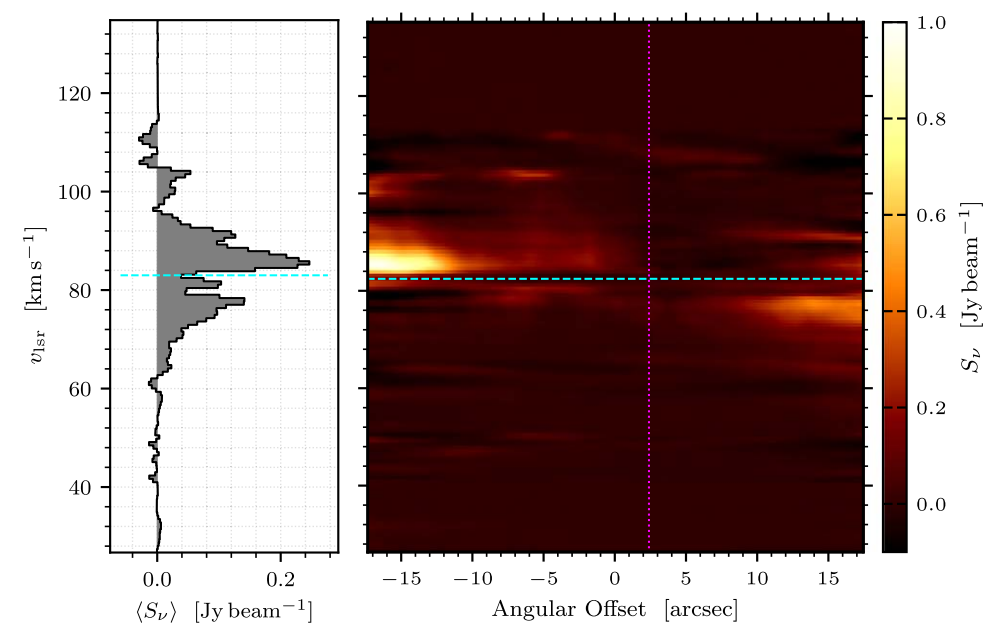


Figure 14. Average spectrum and position–velocity diagram for a 6.00 wide rectangular aperture lying along the outflow axis. Left: spatially averaged spectrum. The center LSR velocity $v_{lsr} = 83.0 \text{ km s}^{-1}$ traced by $H_2CO\ 3_{0,3} \rightarrow 2_{0,2}$ is shown in both panels (cyan dashed line). Right: position–velocity diagram. The peak position of continuum source G24051 S4 is visualized (magenta dotted line).

Appendix B SiO $J = 5 \rightarrow 4$ Maps

Maps of the SiO $J=5 \rightarrow 4$ red- and blueshifted integrated intensities are shown in Figure 15. Three clumps have clear

bipolar outflows: G24051 S5, G28565 S1, and G29601 S1. All three outflows have CO $J=2 \rightarrow 1$ counterparts at similar positions and velocities.

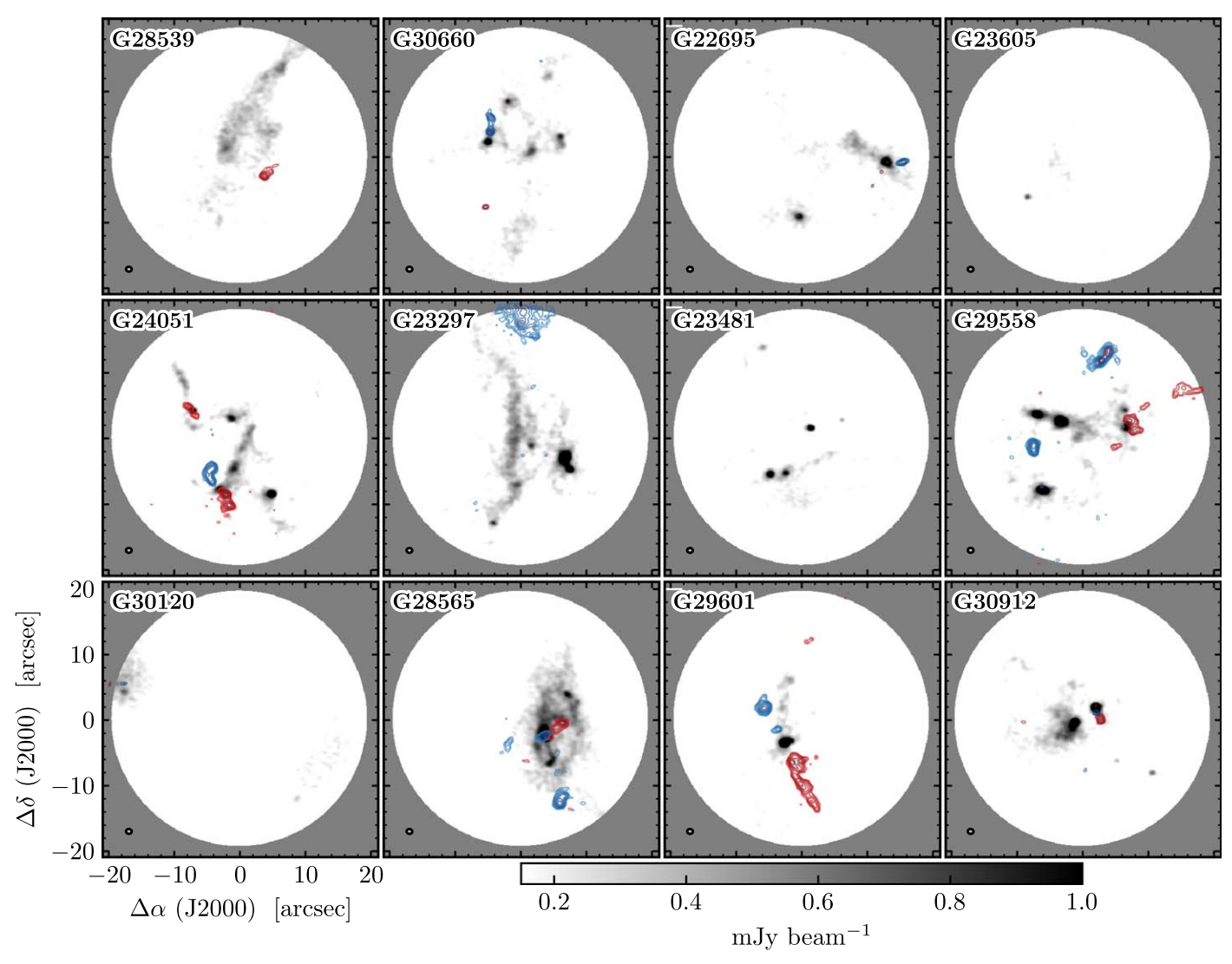


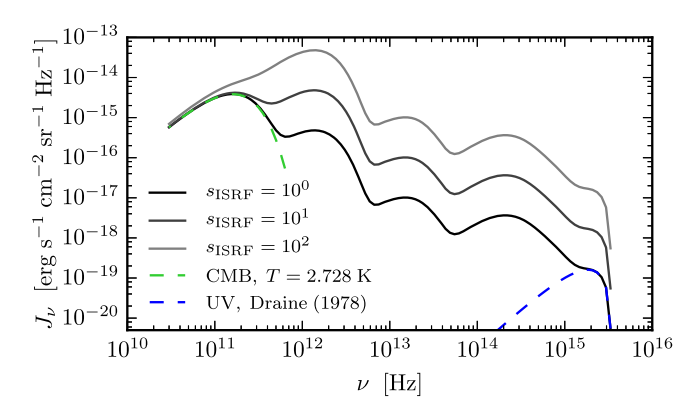
Figure 15. ALMA joint 12 + 7 m array SiO $J = 5 \rightarrow 4$ intensity of velocity components integrated between offsets 2 and 15 km s⁻¹ (red contours) and between offsets -2 and -15 km s⁻¹ (blue contours). Bipolar outflows are observed in 3 out of 12 clumps. Contours are shown at logarithmically spaced steps of 0.050, 0.062, 0.075, 0.093, 0.114, 0.139, 0.171, 0.210, 0.258, and 0.316 Jy km s⁻¹. The inverted grayscale image shows the 230 GHz continuum. The image extends down to the 20% power point (40''). The maps are made from the dirty image cubes and have not been deconvolved with CLEAN.

Appendix C Core Model Properties

We follow an approach to modeling starless cores similar to that found in Shirley et al. (2005) and Lippok et al. (2016). A similar approach is also used in McGuire et al. (2016). We assume dust opacities κ for coagulated grains and thin ice mantles in Ossenkopf & Henning (1994, hereafter OH94) for moderately processed grains with a coagulation timescale of 10^5 yr at densities between 10^4 cm⁻³ to 10^8 cm⁻³ (i.e., "OH4" through "OH6"). The coagulation density $n_{\rm cg}$ from OH94 is selected for each model core based on whether the mean density (weighted by mass) is in the range $0.5 \times n_{\rm cg} - 5 \times n_{\rm cg}$. The value of the dust opacity when interpolated at $\lambda = 1.3$ mm for 10^5 cm⁻³ ("OH5a") is $\kappa = 0.90$ cm² g⁻¹ and varies between 0.51 cm² g⁻¹ to 1.11 cm² g⁻¹ over the full range of densities. We calculate the total gas mass using a dust-to-gas mass ratio of $f_{\rm d} \equiv m_{\rm d}/m_{\rm g} = 1/110$ and an ISM mean

molecular weight of $\mu=2.33$. To fully sample the spectral range of the ISRF, we extrapolate the dust opacities from 1 μ m to 90 nm using the prescription of Cardelli et al. (1989), and from 1.3 mm to 10 mm using the power law $\kappa_{\nu} \propto \nu^{\beta}$ with $\beta=1.75$. In addition, scattering efficiencies for the the OH94 models are added following Young & Evans (2005) and albedos from the Weingartner & Draine (2001) WD3.1 model.

The Plummer-like density profile in Equation (1) is then irradiated in RADMC-3Dwith an external source input using the SED of the ISRF for a self-consistent calculation of the dust temperature distribution. We use the Black (1994) ISRF spectrum as parameterized in Appendix B of Hocuk et al. (2017), with the UV portion of the spectrum adopted from Draine (1978). The ISRF is then varied in relative strength from the local value of the solar neighborhood by a multiplicative factor s_{isrf} , excluding the contribution from the CMB. Figure 16(a) shows the ISRF specific intensity J_{ν} for $s_{isrf} = 10^{0}$, 10^{1} , and 10^{2} , with the five parameterized



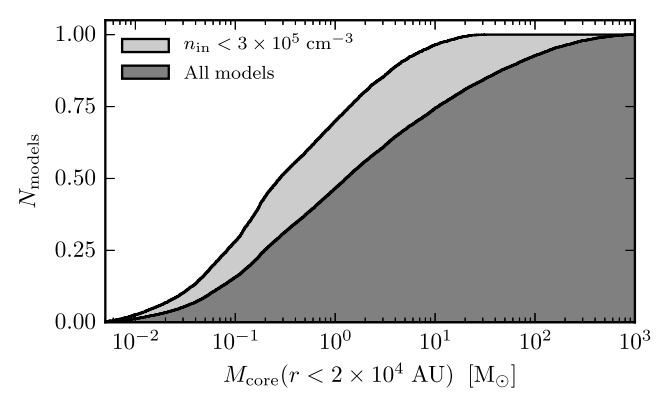


Figure 16. Top: ISRF parameterization used to self-consistently calculate the temperature profiles of starless core radiative transfer models. Flux densities are scaled by factors of 10^0 (black), 10^1 (gray), and 10^2 (light gray), excluding the contribution from the CMB. Bottom: CDF of the gas mass enclosed within a radius of $r < 2 \times 10^4$ au for all models (dark gray) and those with central densities $n_{\rm in} < 3 \times 10^5 \, {\rm cm}^{-3}$ (light gray). The typical core mass is between 0.2 and $20 \, M_{\odot}$.

components clearly visible. Models are computed on a 1D radial grid from 25×10^2 au to 6.0×10^4 au, with 100 zones with 2×10^6 photons to ensure convergence in the output $T_{\rm dust}$ profiles over the tested range in $n_{\rm H}$. The median core mass $M_{\rm core}$ integrated out a radius of 2×10^4 au is $\sim 1~M_{\odot}$, with the (25, 75) percentile interval ranging between $0.2~M_{\odot}$ and $10~M_{\odot}$, extending to $>100~M_{\odot}$ at the 92 percentile. Figure 17 shows the distributions of radial profiles in $n_{\rm H}(r)$, $T_{\rm dust}(r)$, and $S_{\rm 1.3~mm}(\theta)$ at a fiducial distance of 4 kpc. The typical $n_{\rm H}$ at r=10 kau range from $n_{\rm H}=8\times 10^2-3\times 10^5~{\rm cm}^{-3}$ and have typical central $T_{\rm dust}=7-20~{\rm K}$, with the maximum central $T_{\rm dust}=35~{\rm K}$.

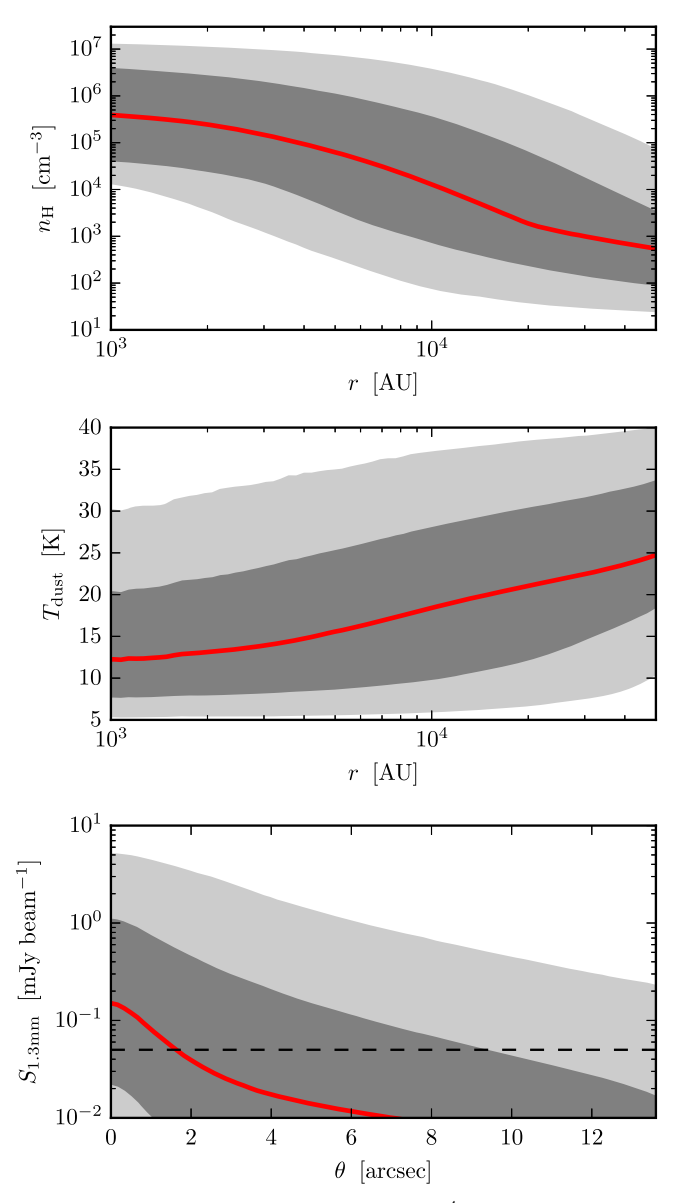


Figure 17. Parameter profiles for the suite of 10^4 models computed with RADMC-3D. For each bin of radii, the median value (red line), 16-84 percentile interval (dark gray region), and 2.5-97.5 percentile interval (light gray region) are shown. Top: input radial gas volume density profiles. Middle: output radial dust temperature profiles varying the ISRF and extinction. Typical central temperatures range from 8 to 20 K. Bottom: output radial surface brightness profiles produced at a fiducial distance of $d_{\odot} = 4$ kpc. The dashed horizontal line indicates the observed image $\sigma_{\rm rms}$.

ORCID iDs

```
Brian E. Svoboda  https://orcid.org/0000-0002-8502-6431 Cara Battersby  https://orcid.org/0000-0002-6073-9320 Gary A. Fuller  https://orcid.org/0000-0001-8509-1818 Qizhou Zhang  https://orcid.org/0000-0003-2384-6589 Henrik Beuther  https://orcid.org/0000-0002-1700-090X Crystal Brogan  https://orcid.org/0000-0002-6558-7653 Todd Hunter  https://orcid.org/0000-0001-6492-0090
```

```
References
Aguirre, J. E., Ginsburg, A. G., Dunham, M. K., et al. 2011, ApJS, 192, 4
André, P., Di Francesco, J., Ward-Thompson, D., et al. 2014, in Protostars and
  Planets VI, ed. H. Beuther et al. (Tucson, AZ: Univ. Arizona Press), 27
Arce, H. G., Shepherd, D., Gueth, F., et al. 2007, in Protostars and Planets V,
   ed. B. Reipurth, D. Jewitt, & K. Keil (Tucson, AZ: Univ. Arizona
   Press), 245
Barnard, E. E. 1907, ApJ, 25, 218
Battersby, C., Bally, J., Jackson, J. M., et al. 2010, ApJ, 721, 222
Battersby, C., Bally, J., & Svoboda, B. 2017, ApJ, 835, 263
Benjamin, R. A., Churchwell, E., Babler, B. L., et al. 2003, PASP, 115, 953
Bergin, E. A., & Tafalla, M. 2007, ARA&A, 45, 339
Beuther, H., Churchwell, E. B., McKee, C. F., & Tan, J. C. 2007, in Protostars
   and Planets V, ed. B. Reipurth, D. Jewitt, & K. Keil (Tucson, AZ: Univ.
   Arizona Press), 165
Beuther, H., Henning, T., Linz, H., et al. 2015a, A&A, 581, A119
Beuther, H., Mottram, J. C., Ahmadi, A., et al. 2018, A&A, 617, 100
Beuther, H., Ragan, S. E., Johnston, K., et al. 2015b, A&A, 584, A67
Black, J. H. 1994, in ASP Conf. Ser. 58, The First Symp. on the Infrared Cirrus
   and Diffuse Interstellar Clouds, ed. R. M. Cutri & W. B. Latter (San
   Francisco, CA: ASP), 355
Bonnell, I. A., Clarke, C. J., Bate, M. R., & Pringle, J. E. 2001, MNRAS,
   324, 573
Bonnor, W. B. 1956, MNRAS, 116, 351
Busquet, G., Estalella, R., Palau, A., et al. 2016, ApJ, 819, 139
Cardelli, J. A., Clayton, G. C., & Mathis, J. S. 1989, ApJ, 345, 245
Carniani, S., Maiolino, R., De Zotti, G., et al. 2015, A&A, 584, A78
Chambers, E. T., Jackson, J. M., Rathborne, J. M., & Simon, R. 2009, ApJS,
   181, 360
Chandrasekhar, S., & Fermi, E. 1953, ApJ, 118, 116
Churchwell, E., Babler, B. L., Meade, M. R., et al. 2009, PASP, 121, 213
Contreras, Y., Schuller, F., Urquhart, J. S., et al. 2013, A&A, 549, A45
Csengeri, T., Urquhart, J. S., Schuller, F., et al. 2014, A&A, 565, A75
Cyganowski, C. J., Brogan, C. L., Hunter, T. R., et al. 2017, MNRAS,
   468, 3694
Cyganowski, C. J., Whitney, B. A., Holden, E., et al. 2008, AJ, 136, 2391
Draine, B. T. 1978, ApJS, 36, 595
Dullemond, C. P., Juhasz, A., Pohl, A., et al. 2012, RADMC-3D: A Multi-
   purpose Radiative Transfer Tool, version 0.41, Astrophysics Source Code
   Library, ascl:1202.015
Dunham, M. M., Stutz, A. M., Allen, L. E., et al. 2014, in Protostars and
   Planets VI, ed. H. Beuther (Tucson, AZ: Univ. Arizona Press), 195
Dzib, S., Loinard, L., Mioduszewski, A. J., et al. 2010, ApJ, 718, 610
Ebert, R. 1955, ZA, 37, 217
Eden, D. J., Moore, T. J. T., Plume, R., et al. 2017, MNRAS, 469, 2163
Elia, D., Molinari, S., Schisano, E., et al. 2017, MNRAS, 471, 100
Ellsworth-Bowers, T. P., Rosolowsky, E., Glenn, J., et al. 2015, ApJ, 799, 29
Enoch, M. L., Corder, S., Duchêne, G., et al. 2011, ApJS, 195, 21
Feng, S., Beuther, H., Zhang, Q., et al. 2016, ApJ, 828, 100
Frank, A., Ray, T. P., Cabrit, S., et al. 2014, in Protostars and Planets VI, ed.
  H. Beuther et al. (Tucson, AZ: Univ. Arizona Press), 451
Friesen, R. K., Bourke, T. L., Di Francesco, J., Gutermuth, R., & Myers, P. C.
   2016, ApJ, 833, 204
Friesen, R. K., Pineda, J. E., co-PIs, et al. 2017, ApJ, 843, 63
Ginsburg, A., Glenn, J., Rosolowsky, E., et al. 2013, ApJS, 208, 14
Hartmann, L., Ballesteros-Paredes, J., & Heitsch, F. 2012, MNRAS, 420, 1457
Hatsukade, B., Ohta, K., Seko, A., Yabe, K., & Akiyama, M. 2013, ApJL,
Hocuk, S., Szucs, L., Caselli, P., et al. 2017, A&A, 604, 58
Hosokawa, T., & Omukai, K. 2009, ApJ, 691, 823
```

Ilee, J. D., Cyganowski, C. J., Nazari, P., et al. 2016, MNRAS, 462, 4386

Inutsuka, S.-I., & Miyama, S. M. 1992, ApJ, 388, 392

Hunter, J. D. 2007, CSE, 9, 90

```
Jackson, J. M., Finn, S. C., Chambers, E. T., Rathborne, J. M., & Simon, R.
  2010, ApJL, 719, L185
Jiménez-Serra, I., Caselli, P., Tan, J. C., et al. 2010, MNRAS, 406, 187
Kainulainen, J., Ragan, S. E., Henning, T., & Stutz, A. 2013, A&A, 557, A120
Kainulainen, J., Stutz, A. M., Stanke, T., et al. 2017, A&A, 600, A141
Kauffmann, J., & Pillai, T. 2010, ApJL, 723, L7
Kong, S., Tan, J. C., Caselli, P., et al. 2017, ApJ, 834, 193
Kroupa, P. 2001, MNRAS, 322, 231
Larson, R. B. 1985, MNRAS, 214, 379
Larson, R. B. 2005, MNRAS, 359, 211
Lippok, N., Launhardt, R., Henning, T., et al. 2016, A&A, 592, A61
Louvet, F., Motte, F., Gusdorf, A., et al. 2016, A&A, 595, A122
Lu, X., Zhang, Q., Wang, K., & Gu, Q. 2015, ApJ, 805, 171
McGuire, C., Fuller, G. A., Peretto, N., et al. 2016, A&A, 594, A118
McKee, C. F., & Ostriker, E. C. 2007, ARA&A, 45, 565
McKee, C. F., & Tan, J. C. 2002, Natur, 416, 59
McKee, C. F., & Tan, J. C. 2003, ApJ, 585, 850
McKinney, W. 2010, in Proc. 9th Python in Science Conf., Data Structures for
   Statistical Computing in Python, ed. S. van der Walt & J. Millman
   (SciPy), 51
McMullin, J. P., Waters, B., Schiebel, D., Young, W., & Golap, K. 2007, in
  ASP Conf. Ser. 376, Astronomical Data Analysis Software and Systems
  XVI, ed. R. A. Shaw, F. Hill, & D. J. Bell (San Francisco, CA: ASP), 127
Molinari, S., Schisano, E., Elia, D., et al. 2016, A&A, 591, A149
Molinari, S., Swinyard, B., Bally, J., et al. 2010, PASP, 122, 314
Motte, F., Bontemps, S., & Louvet, F. 2018, ARA&A, 56, 41
Müller, H. S. P., Schlöder, F., Stutzki, J., & Winnewisser, G. 2005, JMoSt,
  742, 215
Myers, P. C. 2017, ApJ, 838, 10
Nagasawa, M. 1987, PThPh, 77, 635
Nguyen-Lu'o'ng, Q., Motte, F., Carlhoff, P., et al. 2013, ApJ, 775, 88
Oliphant, T. E. 2007, CSE, 9, 10
Ossenkopf, V., & Henning, T. 1994, A&A, 291, 943
Ostriker, J. 1964, ApJ, 140, 1056
Palau, A., Ballesteros-Paredes, J., Vázquez-Semadeni, E., et al. 2015, MNRAS,
  453, 3785
Palau, A., Zapata, L. A., Roman-Zuniga, C. G., et al. 2018, ApJ, 855, 24
Peretto, N., & Fuller, G. A. 2009, A&A, 505, 405
Pérez, F., & Granger, B. E. 2007, CSE, 9, 21
Peters, T., Banerjee, R., Klessen, R. S., et al. 2010a, ApJ, 711, 1017
Peters, T., Banerjee, R., Klessen, R. S., & Mac Low, M.-M. 2011, ApJ, 729, 72
Peters, T., Klessen, R. S., Mac Low, M.-M., & Banerjee, R. 2010b, ApJ,
  725, 134
Plummer, H. C. 1911, MNRAS, 71, 460
Pokhrel, R., Myers, P. C., Dunham, M. M., et al. 2018, ApJ, 853, 5
Remijan, A. J., Markwick-Kemper, A., & Working, A. L. M. A. 2007, AAS
  Meeting, 211, 132.11
Robitaille, T. P. 2017, A&A, 600, A11
Robitaille, T. P., Whitney, B. A., Indebetouw, R., & Wood, K. 2007, ApJS,
  169, 328
Rosero, V., Hofner, P., Claussen, M., et al. 2016, ApJS, 227, 25
Rosolowsky, E., Dunham, M. K., Ginsburg, A., et al. 2010, ApJS, 188, 123
Rosolowsky, E. W., Pineda, J. E., Kauffmann, J., & Goodman, A. A. 2008,
   ApJ, 679, 1338
Sanhueza, P., Jackson, J. M., Foster, J. B., et al. 2013, ApJ, 773, 123
Sanhueza, P., Jackson, J. M., Zhang, Q., et al. 2017, ApJ, 841, 97
Sato, M., Wu, Y. W., Immer, K., et al. 2014, ApJ, 793, 72
Schilke, P., Walmsley, C. M., Pineau des Forets, G., & Flower, D. R. 1997,
  A&A, 321, 293
Schuller, F., Menten, K. M., Contreras, Y., et al. 2009, A&A, 504, 415
Shirley, Y. L., Claussen, M. J., Bourke, T. L., Young, C. H., & Blake, G. A.
   2007, ApJ, 667, 329
Shirley, Y. L., Nordhaus, M. K., Grcevich, J. M., et al. 2005, ApJ, 632, 982
Smith, R. J., Glover, S. C. O., Klessen, R. S., & Fuller, G. A. 2016, MNRAS,
Smith, R. J., Longmore, S., & Bonnell, I. 2009, MNRAS, 400, 1775
Svoboda, B. E., Shirley, Y. L., Battersby, C., et al. 2016, ApJ, 822, 59
Tan, J. C., Beltrán, M. T., Caselli, P., et al. 2014, in Protostars and Planets VI,
  ed. H. Beuther et al. (Tucson, AZ: Univ. Arizona Press), 149
Tan, J. C., Kong, S., Butler, M. J., Caselli, P., & Fontani, F. 2013, ApJ, 779, 96
Tan, J. C., Kong, S., Zhang, Y., et al. 2016, ApJL, 821, L3
Teixeira, P. S., Takahashi, S., Zapata, L. A., & Ho, P. T. P. 2016, A&A,
  587. A47
The Astropy Collaboration, Price-Whelan, A. M., Sipőcz, B. M., et al. 2018,
   AJ, 156, 123
Traficante, A., Fuller, G. A., Billot, N., et al. 2017, MNRAS, 470, 3882
```

651, L125

```
Traficante, A., Fuller, G. A., Peretto, N., Pineda, J. E., & Molinari, S. 2015, MNRAS, 451, 3089
Veneziani, M., Elia, D., Noriega-Crespo, A., et al. 2013, A&A, 549, A130
Wang, K., Zhang, Q., Testi, L., et al. 2014, MNRAS, 439, 3275
Wang, K., Zhang, Q., Wu, Y., Li, H.-b., & Zhang, H. 2012, ApJL, 745, L30
Wang, K., Zhang, Q., Wu, Y., & Zhang, H. 2011, ApJ, 735, 64
Wang, P., Li, Z.-Y., Abel, T., & Nakamura, F. 2010, ApJ, 709, 27
```

Wang, Y., Zhang, Q., Rathborne, J. M., Jackson, J., & Wu, Y. 2006, ApJL,

```
Weingartner, J. C., & Draine, B. T. 2001, ApJ, 548, 296
Whitworth, A. P., & Ward-Thompson, D. 2001, ApJ, 547, 317
Wienen, M., Wyrowski, F., Schuller, F., et al. 2012, A&A, 544, A146
Williams, J. P., de Geus, E. J., & Blitz, L. 1994, ApJ, 428, 693
Young, C. H., & Evans, N. J., II 2005, ApJ, 627, 293
Yuan, J., Wu, Y., Ellingsen, S. P., et al. 2017, ApJS, 231, 11
Zhang, Q., & Wang, K. 2011, ApJ, 733, 26
Zhang, Q., Wang, K., Lu, X., & Jiménez-Serra, I. 2015, ApJ, 804, 141
Zhang, Q., Wang, Y., Pillai, T., & Rathborne, J. 2009, ApJ, 696, 268
Zhang, Y., Tan, J. C., & Hosokawa, T. 2014, ApJ, 788, 166
```